

Gradient damage modeling of brittle fracture in an explicit dynamics context

Tianyi Li^{1,*†}, Jean-Jacques Marigo², Daniel Guilbaud^{1,3} and Serguei Potapov^{1,4}

¹*Institute of Mechanical Sciences and Industrial Applications, UMR EDF-CNRS-CEA-ENSTA ParisTech 9219, Université Paris Saclay, 828 boulevard des Maréchaux, 91762 Palaiseau Cedex, France*

²*Laboratoire de Mécanique des Solides, École Polytechnique, 91128 Palaiseau Cedex, France*

³*DEN-Service d'Etudes Mécaniques et Thermiques (SEMT), CEA Saclay, 91191 Gif-sur-Yvette Cedex, France*

⁴*EDF Lab Paris-Saclay, 7 boulevard Gaspard Monge, 91120 Palaiseau, France*

SUMMARY

In this contribution, we propose a dynamic gradient damage model as a phase-field approach for studying brutal fracture phenomena in quasi-brittle materials under impact-type loading conditions. Several existing approaches to account for the tension–compression asymmetry of fracture behavior of materials are reviewed. A better understanding of these models is provided through a uniaxial traction experiment. We then give an efficient numerical implementation of the model in an explicit dynamics context. Simulations results obtained with parallel computing are discussed both from a computational and physical point of view. Different damage constitutive laws and tension–compression asymmetry formulations are compared with respect to their aptitude to approximate brittle fracture. Copyright © 2016 John Wiley & Sons, Ltd.

Received 23 December 2015; Revised 24 March 2016; Accepted 31 March 2016

KEY WORDS: gradient damage models; dynamic fracture; variational methods; explicit dynamics

1. INTRODUCTION

Phase-field modeling of dynamic fracture is gaining popularity over the last few years within the computational mechanics community [1–5]. From a physical point of view, it is based on the variational approach to fracture and its elliptic regularization [6], which frees itself from several limitations inherent to the Griffith's theory: an initial crack and a given path. It settles down a unified framework covering the onset and the space-time propagation of cracks with possible complex topologies. A mere retranslation of Griffith's original idea, the variational formulation focuses on global energetic quantities and sees the crack evolution as a minimization movement of the sum of the stored elastic energy and the crack surface energy. Nucleation of defects in an initially sound domain as well as kinking, branching, or coalescence of cracks naturally follow the competition of the involved energies. From a computational point of view, the introduction of a continuous phase field regularizes the sharp interface description of cracks, which renders unnecessary an explicit algorithmic tracking of the crack surface and the current crack front in two-dimensional and three-dimensional cases. Crack tip singularities automatically disappear because of regularization, and the classical finite element method can be used throughout the domain, as long as the regularized crack geometries are correctly captured by a relatively small mesh size. Because of these advantages, phase-field models can be used to explore numerous dynamic fracture phenomena in particular crack instabilities [7] or as a tool for experimental validations [8].

*Correspondence to: T. Li, IMSIA, UMR EDF-CNRS-CEA-ENSTA ParisTech 9219, Université Paris-Saclay, 828 boulevard des Maréchaux, 91762 Palaiseau Cedex, France

†E-mail: tianyi.li@polytechnique.edu

Meanwhile, the regularized phase-field formulation of fracture [6] can be acknowledged as a genuine gradient damage model *per se* ([9–11]), where the regularization parameter contributes to the fracture or damage behavior of materials. The link between the gradient damage model and the Griffith's theory of fracture without using global minimization arguments (Γ -convergence theory for instance) is established in [12] for quasi-static situations. Its dynamic extension has been accomplished and will be the object of another contribution. Based on shape derivative techniques and an adaptation of the variational principles, a generalized Griffith's law is obtained, which governs the crack tip equation of motion. When the material internal length is sufficiently small compared with the typical length of the structure, a separation of scales can be achieved in an asymptotic context. In that case, crack propagation in a gradient damage medium results from the competition between the energy release rate of the outer linear elastic fracture mechanics problem and the fracture toughness identified as the energy consumed during the damage band creation. Numerical verification of these theoretic ideas is conducted in [13] for an antiplane tearing experiment of a two-dimensional plate. The dynamic crack evolution obtained with the gradient damage model agrees well with the fracture mechanics predictions, both in absence and in presence of material inhomogeneities. The generalized energy release rates can be seen as a theoretical and numerical tool to establish the transition from damage to fracture.

In this contribution, we propose to strengthen the bridge between the phase-field and the gradient damage communities in order to achieve a better modeling of brittle dynamic fracture. We give a review of several existing approaches in both communities to account for the tension–compression asymmetry of fracture behavior of materials. A better understanding and comparison of these physical models is provided through analytical studies of a uniaxial traction experiment and their applications to real fracture problems. We also recognize the widely used regularized surface density function in the phase-field description of cracks as a special choice for the damage constitutive laws. The physical properties of these functions have been analytically studied in [11, 14, 15]. Here, through concrete numerical simulations of dynamic fracture problems, we compare different damage constitutive laws with respect to their aptitude with approximate fracture, from both the computational and physical points of view.

This paper is organized as follows. The variational formulation of the dynamic gradient damage model is proposed in Section 2. A review of several existing tension–compression asymmetry models is provided in Section 3, where they are compared in a uniaxial traction experiment. Section 4 is devoted to the spatial and temporal discretization of the model in an explicit dynamics context. We then discuss in Section 5 the simulation results, which illustrate the differences of the previously presented damage constitutive laws and tension–compression asymmetry formulations. An experimental validation of the proposed model is also described. Finally, some conclusions on the use of gradient damage models to approximate dynamic brittle fracture can be found in Section 6.

General notation conventions adopted in this paper are summarized as follows. Scalar-valued quantities will be denoted by italic Roman or Greek letters like the crack length l_t or the damage field α_t . Vectors and higher order tensors will be represented by boldface letters such as the displacement field \mathbf{u}_t and the elasticity tensor \mathbf{A} for instance. Intrinsic notation is adopted, and contraction on lower-order tensors will be written without dots $\mathbf{A}\boldsymbol{\varepsilon} = \mathbf{A}_{ijkl}\boldsymbol{\varepsilon}_{kl}$. Inner products between two vectors or tensors of the same order will be denoted with a dot, such as $\mathbf{A}\boldsymbol{\varepsilon} \cdot \boldsymbol{\varepsilon} = \mathbf{A}_{ijkl}\boldsymbol{\varepsilon}_{kl}\boldsymbol{\varepsilon}_{ij}$. Time dependence will be noted at the subscripts of the involved quantities, like $\mathbf{u} : (t, \mathbf{x}) \mapsto \mathbf{u}_t(\mathbf{x})$.

2. VARIATIONAL FRAMEWORK

The governing equations of the dynamic gradient damage model can be encapsulated into a purely variational framework thanks to the definition of a space-time action integral of several scalar energetic quantities of the structure ([3, 13]). Cracks are located with the help of a scalar damage field $0 \leq \alpha \leq 1$ in a two-dimensional or three-dimensional domain Ω (cf. Figure 1). This field depicts a smooth transition between the undamaged part of the structure $\alpha = 0$ and the crack $\alpha = 1$ and, thus, can be considered as an isotropic phase-field indicator.

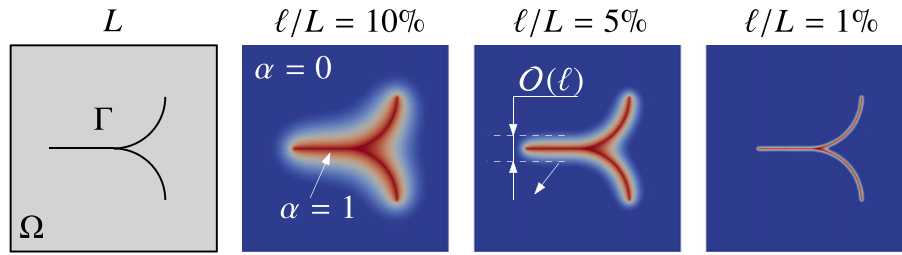


Figure 1. The discrete crack $\Gamma \subset \Omega$ approximated by a continuous damage field $0 \leq \alpha \leq 1$.

Given arbitrary admissible displacement, velocity and damage fields $(\mathbf{u}_t, \dot{\mathbf{u}}_t, \alpha_t)$, the energetic quantities needed in the variational formulation are defined as follows. We place ourselves under the small displacement theory. This is a plausible model for brittle materials when large rotations are also not expected. Assuming this hypothesis, the elastic energy is given by

$$\mathcal{E}(\mathbf{u}_t, \alpha_t) = \int_{\Omega} \psi(\boldsymbol{\varepsilon}(\mathbf{u}_t), \alpha_t) \, \mathrm{d}\mathbf{x} = \int_{\Omega} a(\alpha_t) \psi_0(\boldsymbol{\varepsilon}(\mathbf{u}_t)) \, \mathrm{d}\mathbf{x} = \int_{\Omega} \frac{1}{2} a(\alpha_t) \mathbf{A} \boldsymbol{\varepsilon}(\mathbf{u}_t) \cdot \boldsymbol{\varepsilon}(\mathbf{u}_t) \, \mathrm{d}\mathbf{x} \quad (1)$$

where \mathbf{A} is the standard isotropic Hooke's elasticity tensor, $\boldsymbol{\varepsilon}$ the symmetrized gradient operator, which gives the linearized strain $\boldsymbol{\varepsilon}(\mathbf{u}_t) = \frac{1}{2}(\nabla \mathbf{u}_t + \nabla^T \mathbf{u}_t)$ when applied to the displacement vector, and $\alpha \mapsto a(\alpha)$ an adimensional damage constitutive function describing stiffness degradation in the bulk. This function should verify certain physical properties discussed in [11] for the gradient damage model to appropriately approximate brittle fracture. The exact form of this function considered in this contribution will be specified at the end of this section. The stress tensor derived from (1) is thus given by $\boldsymbol{\sigma}_t = a(\alpha_t) \mathbf{A} \boldsymbol{\varepsilon}(\mathbf{u}_t)$. To simplify the formulation, we can observe that here, the function $a(\alpha)$ acts symmetrically on the sound elastic energy density ψ_0 and the stress tensor. Generalization to include tension–compression asymmetry should not influence the variational formulation proposed here and hence will be discussed in Section 3. Concerning the kinetic energy, it is defined as usual by

$$\mathcal{K}(\dot{\mathbf{u}}_t) = \int_{\Omega} \frac{1}{2} \rho \dot{\mathbf{u}}_t \cdot \dot{\mathbf{u}}_t \, \mathrm{d}\mathbf{x}. \quad (2)$$

No damage dependence is considered here, and thus, the total mass is conserved. We now turn to the definition of the damage dissipation energy, which quantifies the amount of energy consumed in the damage process. According to the Γ -convergence theory [6], this energy is closely related to the Griffith-like surface energy of cracks and hence can be used to deduce the total crack surface area. We will use the same definition given in [11] for quasi-static calculations (with a non-essential rescaling of the internal length $\ell \mapsto \sqrt{2}\ell$) because it is clear that dynamics do not play a role here

$$\mathcal{S}(\alpha_t) = \int_{\Omega} (w(\alpha_t) + w_1 \ell^2 \nabla \alpha_t \cdot \nabla \alpha_t) \, \mathrm{d}\mathbf{x}. \quad (3)$$

Because of the presence of the gradient term, the damage dissipation mechanism becomes non-local, and localization is systematically accompanied by finite energy consumption. In (3), the function $\alpha \mapsto w(\alpha)$ is another damage constitutive law representing the local energy dissipation during a homogeneous damage evolution, and its maximal value $w(1) = w_1$ is the energy completely dissipated during such process. This function along with the former stiffness degradation function $a(\alpha)$ characterizes the damage constitutive behavior of the material and should also satisfy certain physical properties [11], which we do not reproduce here. The exact form of this function will also be specified at the end of this section. The internal length ℓ , as can be seen in Figure 1, controls the width of the damage band. It can be regarded as a purely numerical parameter, which should be

chosen as small as possible ([6]). However, its role as a material parameter is now fully recognized [11, 16]. An effective fracture toughness G_c , that is, the energy required to create a unit Griffith-like crack surface, can be identified as the energy dissipated during the optimal damage band creation

$$G_c = 4\ell \int_0^1 \sqrt{w_1 w(\beta)} d\beta \quad (4)$$

and (4) prescribes a relation between the fracture toughness G_c , the total energy dissipation due to damage w_1 , and the internal length ℓ . We refer the readers to [11] for a more detailed discussion on the relationship between these gradient damage and fracture parameters.

Before announcing the governing equations of the gradient damage model, we need to specify the loading conditions the body Ω is subject to as well as the admissible spaces for the displacement and the damage evolutions in which the aforementioned energies (1)–(3) can be defined. Body forces \mathbf{f}_t and surface tractions \mathbf{F}_t on a subset of the boundary $\partial\Omega_F$ are applied to the structure and will be characterized by an external potential

$$\mathcal{W}_t(\mathbf{u}_t) = \int_{\Omega} \mathbf{f}_t \cdot \mathbf{u}_t d\mathbf{x} + \int_{\partial\Omega_F} \mathbf{F}_t \cdot \mathbf{u}_t d\mathbf{s}. \quad (5)$$

On a subset $\partial\Omega_U$ of the boundary, the body is subject to a prescribed displacement $t \mapsto \mathbf{U}_t$, which is built into the definition of the admissible displacement space \mathcal{C}_t . We suppose that it is an affine space of form $\mathcal{C}_t = \mathcal{C}_0 + \mathbf{U}_t$ where \mathcal{C}_0 is the associated vector space given by

$$\mathcal{C}_0 = \{\mathbf{u}_t: \Omega \rightarrow \mathbb{R}^{\dim} | \mathbf{u}_t = \mathbf{0} \text{ on } \partial\Omega_U\}$$

in which the regularity condition is implicitly supposed. The admissible damage space will be built from an arbitrary damage state $0 \leq \alpha_t \leq 1$, and it is defined by

$$\mathcal{D}(\alpha_t) = \{\beta_t: \Omega \rightarrow [0, 1] | 0 \leq \alpha_t \leq \beta_t \leq 1\}. \quad (6)$$

It can be seen that a virtual damage field β_t is admissible, if and only if it is accessible from the current damage state α_t verifying the irreversibility condition, that is, the damage only grows. In order to use the Hamilton's principle for an arbitrary interval of time of interest $I = [0, T]$, we construct the following admissible evolution spaces

$$\mathcal{C}(\mathbf{u}) = \{\mathbf{v}: I \times \Omega \rightarrow \mathbb{R}^{\dim} | \mathbf{v}_t \in \mathcal{C}_t \text{ for all } t \in I \text{ and } \mathbf{v}_{\partial I} = \mathbf{u}_{\partial I}\}$$

and

$$\mathcal{D}(\alpha) = \{\beta: I \times \Omega \rightarrow \mathbb{R} | \beta_t \in \mathcal{D}(\alpha_t) \text{ for all } t \in I \text{ and } \beta_{\partial I} = \alpha_{\partial I}\}$$

by fixing the values of these two fields at both time ends denoted by $\mathbf{u}_{\partial I} = (\mathbf{u}_0, \mathbf{u}_T)$ and $\alpha_{\partial I} = (\alpha_0, \alpha_T)$. With all the variational ingredients set, we are now in a position to form the space-time action integral given by

$$\mathcal{A}(\mathbf{u}, \alpha) = \int_I \mathcal{L}_t(\mathbf{u}_t, \dot{\mathbf{u}}_t, \alpha_t) dt = \int_I \mathcal{E}(\mathbf{u}_t, \alpha_t) + \mathcal{S}(\alpha_t) - \mathcal{K}(\dot{\mathbf{u}}_t) - \mathcal{W}_t(\mathbf{u}_t) dt$$

and announce the following

Model 1 (Dynamic gradient damage evolution law)

The coupled two-field (\mathbf{u}, α) time-continuous dynamic gradient damage problem is governed by the following physical principles

1. Irreversibility: the damage $t \mapsto \alpha_t$ is a non-decreasing function of time.
2. First-order stability: the first-order action variation is non-negative with respect to arbitrary admissible displacement and damage evolutions

$$\mathcal{A}'(\mathbf{u}, \alpha)(\mathbf{v} - \mathbf{u}, \beta - \alpha) \geq 0 \text{ for all } \mathbf{v} \in \mathcal{C}(\mathbf{u}) \text{ and all } \beta \in \mathcal{D}(\alpha). \quad (7)$$

3. Energy balance: the only energy dissipation is due to damage

$$\mathcal{H}_t = \mathcal{H}_0 + \int_0^t \left(\int_{\Omega} (\boldsymbol{\sigma}_s \cdot \boldsymbol{\varepsilon}(\dot{\mathbf{u}}_s) + \rho \ddot{\mathbf{u}}_s \cdot \dot{\mathbf{u}}_s) \, d\mathbf{x} - \mathcal{W}_s(\dot{\mathbf{u}}_s) - \dot{\mathcal{W}}_s(\mathbf{u}_s) \right) \, ds \quad (8)$$

where the total energy is defined by

$$\mathcal{H}_t = \mathcal{E}(\mathbf{u}_t, \alpha_t) + \mathcal{S}(\alpha_t) + \mathcal{K}(\dot{\mathbf{u}}_t) - \mathcal{W}_t(\mathbf{u}_t).$$

Further physical insights can be gained from the very compact first-order stability condition (7) written as a variational inequality. By developing the directional derivative of the action integral at fixed damage evolutions $\beta = \alpha$ and supposing that the displacement field is sufficiently regular in time, the weak dynamic linear momentum equilibrium can be derived. Denoting the variation $\mathbf{v} - \mathbf{u}$ by \mathbf{w} , we obtain after an integration by parts in the time domain

$$\mathcal{A}'(\mathbf{u}, \alpha)(\mathbf{w}, 0) = \int_I dt \int_{\Omega} (\boldsymbol{\sigma}_t \cdot \boldsymbol{\varepsilon}(\mathbf{w}_t) + \rho \ddot{\mathbf{u}}_t \cdot \mathbf{w}_t) \, d\mathbf{x} - \mathcal{W}_t(\mathbf{w}_t) = 0 \text{ for all } \mathbf{w}_t \in \mathcal{C}_0$$

where the equality $\mathcal{A}'(\mathbf{u}, \alpha)(\mathbf{w}, 0) = 0$ follows given that \mathcal{C}_0 is a vector space. We recall that here, the stress tensor is modulated by the stiffness degradation function and is given by $\boldsymbol{\sigma}_t = a(\alpha_t) \mathbf{A} \boldsymbol{\varepsilon}(\mathbf{u}_t)$. The arbitrariness of the temporal variation of \mathbf{w} leads thus to the desired weak elastodynamic equation

$$\int_{\Omega} (\boldsymbol{\sigma}_t \cdot \boldsymbol{\varepsilon}(\mathbf{w}_t) + \rho \ddot{\mathbf{u}}_t \cdot \mathbf{w}_t) \, d\mathbf{x} - \mathcal{W}_t(\mathbf{w}_t) = 0 \text{ for all } \mathbf{w}_t \in \mathcal{C}_0. \quad (9)$$

As for the governing equation for damage evolution, we observe that time dependence of damage is introduced solely via the irreversibility condition and the admissible damage evolution space $\mathcal{D}(\alpha)$. Using the fundamental lemma of calculus of variations in the time domain and the fact that $\mathcal{D}(\alpha_t)$ defined in (6) is convex, the first-order stability condition tested with $\mathbf{v} = \mathbf{u}$ results in the partial minimality of the total energy with respect to the damage variable under the irreversible constraint

$$\mathcal{E}(\mathbf{u}_t, \alpha_t) + \mathcal{S}(\alpha_t) \leq \mathcal{E}(\mathbf{u}_t, \beta_t) + \mathcal{S}(\beta_t) \text{ for all } \beta_t \in \mathcal{D}(\alpha_t). \quad (10)$$

The same energy minimization principle holds also for quasi-static gradient damage models [11]; however, here, the displacement field \mathbf{u}_t follows the elastodynamic equation (9). In this work, we will fully exploit the variational nature of the damage problem, and (10) will be numerically solved by a direct mathematical optimization procedure at the structural scale. For the equivalent local conditions of the damage criterion (10) and the energy balance condition (8), readers are referred to [12].

While other sophisticated constitutive functions exist (for instance those proposed and analytically studied in [14, 15]), in this work, we will consider two particular damage constitutive laws. Their use for phase-field modeling of cracks will be studied through numerical experiments in the sequel. They both involve only polynomial functions of the damage up to degree 2; thus, the elastic energy \mathcal{E} and the damage dissipation energy \mathcal{S} are quadratic with respect to damage, a rather interesting property from a computational cost point of view because the Hessian matrix is constant.

- The Pham, Amor, Marigo, and Maurini model with an elastic domain initially introduced in [11] and named after their initials. Damage does not evolve as long as a critical stress is not reached, a rather appreciated property when modeling brittle fracture. Then a stress-softening behavior is observed as damage grows, where the cubic and the quartic constitutive functions proposed by [17] still possess a small stress-hardening interval.

$$a(\alpha) = (1 - \alpha)^2, \quad w(\alpha) = w_1 \alpha. \quad (\text{PAMM})$$

- The original Ambrosio and Tortorelli regularization model introduced in [18]. The quadratic growing damage dissipation function $\alpha \mapsto w(\alpha)$ is used in many phase-field models of fracture [1–3]. This can be seen by calculating the maximal damage dissipation w_1 as a function of the fracture toughness G_c by (4). This constitutive function will be compared with (PAMM) through numerical simulations in Section 5.

$$a(\alpha) = (1 - \alpha)^2, \quad w(\alpha) = w_1 \alpha^2. \quad (\text{AT})$$

3. TENSION–COMPRESSION ASYMMETRY

In this section, we will discuss several approaches in an attempt to account for the tension–compression asymmetry of damage behavior of materials. The objective is to provide a better understanding of the existing models following a theoretical approach and to point out some improvements that can be carried out in the future.

3.1. Review of existing models

In general, two possibilities can be considered: modification of damage dependence of the elastic energy (1) and/or modification of the variational principles (of irreversibility, stability, and energy balance) outlined in Model 1. The second approach has been discussed in [4, 19] where the damage driving force $\partial_\alpha \psi(\boldsymbol{\varepsilon}_t, \alpha_t)$ deduced from the energy minimization principle (10) is replaced by, for example, some stress-based criteria in presence of a damage threshold function. However, it is known from [12] that the variational formulation plays an essential role in establishing the link between damage and fracture and in the definition of a generalized energy release rate with respect to the crack extension. That is why, only the first possibility will be discussed in this paper. For notational simplicity, we place ourselves at a particular material point \mathbf{x} characterized by a strain tensor $\boldsymbol{\varepsilon} = \boldsymbol{\varepsilon}(\mathbf{u}_t)(\mathbf{x})$ and a current damage state $\alpha = \alpha_t(\mathbf{x})$.

Several existing approaches consist of additively partitioning the sound elastic energy density $\psi_0(\boldsymbol{\varepsilon})$ in (1) into two parts: a *positive* part $\psi_0^+(\boldsymbol{\varepsilon})$, which is considered to contribute to damage, and the *negative* part $\psi_0^-(\boldsymbol{\varepsilon})$, which resists to damage. The elastic energy density in (1) being acted symmetrically in tension and compression by damage is then replaced by the expression

$$\psi(\boldsymbol{\varepsilon}, \alpha) = a(\alpha)\psi_0^+(\boldsymbol{\varepsilon}) + \psi_0^-(\boldsymbol{\varepsilon}) \quad (11)$$

where the damage degradation function $a(\alpha)$ only acts on the positive part $\psi_0^+(\boldsymbol{\varepsilon})$. By doing so, damage evolution is then driven by the positive elastic energy according to (10). In this contribution, we will adopt this additive partition approach because only small strains are expected for brittle materials. In the finite strain regime, a multiplicative decomposition of the deformation gradient \mathbf{F}_t could be a more suitable alternative [20] for allowing fracture only under tension.

Furthermore, if the partition of the sound elastic energy $\psi_0(\boldsymbol{\varepsilon})$ is based on that of the strain tensor $\boldsymbol{\varepsilon} = \boldsymbol{\varepsilon}^+ + \boldsymbol{\varepsilon}^-$, that is, the constitutive behaviors

$$\begin{aligned} \boldsymbol{\varepsilon}^\pm &\mapsto \psi_0^\pm(\boldsymbol{\varepsilon}^\pm) = \frac{1}{2} \mathbf{A} \boldsymbol{\varepsilon}^\pm \cdot \boldsymbol{\varepsilon}^\pm, \\ \boldsymbol{\varepsilon}^\pm &\mapsto \boldsymbol{\sigma}_0^\pm(\boldsymbol{\varepsilon}^\pm) = \mathbf{A} \boldsymbol{\varepsilon}^\pm \end{aligned} \quad (12)$$

are characterized by the same elasticity tensor \mathbf{A} both for the positive and negative strains, then there exists in fact a local variational principle from which several existing tension–compression asymmetry models can be derived. This formulation is adapted from [10] where the framework of structured deformations is used to decompose the strain tensor into an elastic part and an inelastic one related to microstructures, which in our notation, is given by $\alpha \boldsymbol{\varepsilon}^+$. However, here, we confine ourselves to macroscopic modeling and interpret the positive strain $\boldsymbol{\varepsilon}^+$ as the part that merely contributes to

local material degradation. The mechanical modeling of such positive strains will be encapsulated into a convex subset \mathcal{S} of the symmetrized second-order tensor. The actual computation of $\boldsymbol{\varepsilon}^+ \in \mathcal{S}$ is determined by the following local variational requirement for every material point

$$\|\boldsymbol{\varepsilon}^+ - \boldsymbol{\varepsilon}\|_{\mathbf{A}} = \min_{\mathbf{e} \in \mathcal{S}} \|\mathbf{e} - \boldsymbol{\varepsilon}\|_{\mathbf{A}} = \min_{\mathbf{e} \in \mathcal{S}} \mathbf{A}(\boldsymbol{\varepsilon} - \mathbf{e}) \cdot (\boldsymbol{\varepsilon} - \mathbf{e}). \quad (13)$$

Owing to the convexity of \mathcal{S} , the positive strain $\boldsymbol{\varepsilon}^+$ is unique and is defined as the orthogonal projection of the total strain $\boldsymbol{\varepsilon}$ onto the space \mathcal{S} with respect to the energy norm defined by the elasticity tensor \mathbf{A} . From convex analysis, it is known that $\boldsymbol{\varepsilon}^+$, which satisfies (13), can be equivalently characterized by

$$-\mathbf{A}(\boldsymbol{\varepsilon} - \boldsymbol{\varepsilon}^+) \cdot (\mathbf{e} - \boldsymbol{\varepsilon}^+) \geq 0 \text{ for all } \mathbf{e} \in \mathcal{S}, \quad (14)$$

which implies from the definition (12) that the negative sound stress $\boldsymbol{\sigma}_0^- = \mathbf{A}\boldsymbol{\varepsilon}^-$ is in the polar cone $\mathcal{S}^* = \{\mathbf{e}^* | \mathbf{e}^* \cdot \mathbf{e} \leq 0 \text{ for all } \mathbf{e} \in \mathcal{S}\}$. If the space \mathcal{S} is also a cone, that is closed with respect to arbitrary positive rescaling $\alpha \mathbf{e}$ for $\alpha > 0$, then testing (14) with $\mathbf{e} = 2\boldsymbol{\varepsilon}^+$ and $\mathbf{e} = \frac{1}{2}\boldsymbol{\varepsilon}^+$ furnishes along with the symmetry of \mathbf{A} the following orthogonality conditions

$$\begin{aligned} \boldsymbol{\sigma}_0^- \cdot \boldsymbol{\varepsilon}^+ &= \mathbf{A}(\boldsymbol{\varepsilon} - \boldsymbol{\varepsilon}^+) \cdot \boldsymbol{\varepsilon}^+ = 0, \\ \boldsymbol{\sigma}_0^+ \cdot \boldsymbol{\varepsilon}^- &= \mathbf{A}(\boldsymbol{\varepsilon} - \boldsymbol{\varepsilon}^-) \cdot \boldsymbol{\varepsilon}^- = 0. \end{aligned} \quad (15)$$

This implies that ψ_0^+ and ψ_0^- defined in (12) constitute indeed a partition of the sound elastic energy density

$$2\psi_0(\boldsymbol{\varepsilon}) = \mathbf{A}\boldsymbol{\varepsilon} \cdot \boldsymbol{\varepsilon} = \boldsymbol{\sigma}_0^+ \cdot \boldsymbol{\varepsilon}^+ + \boldsymbol{\sigma}_0^- \cdot \boldsymbol{\varepsilon}^-$$

where the crossed terms disappear thanks to (15). This provides another interpretation of (13) from a mechanical point of view: the positive part of the strain minimizes the negative part of the elastic energy $\boldsymbol{\sigma}_0^- \cdot \boldsymbol{\varepsilon}^-$ that resists to damage.

We now turn to the stress tensor derived from (11) and (12). In general, we should have by definition

$$\boldsymbol{\sigma}(\boldsymbol{\varepsilon}, \alpha)\mathbf{e} = a(\alpha)\boldsymbol{\sigma}_0^+ \cdot \frac{\partial \boldsymbol{\varepsilon}^+}{\partial \boldsymbol{\varepsilon}}(\boldsymbol{\varepsilon})\mathbf{e} + \boldsymbol{\sigma}_0^- \cdot \frac{\partial \boldsymbol{\varepsilon}^-}{\partial \boldsymbol{\varepsilon}}(\boldsymbol{\varepsilon})\mathbf{e} \quad (16)$$

where derivatives of the decomposed strains $\boldsymbol{\varepsilon}^\pm$ with respect to the total strain appear. Fortunately, as $\partial_{\boldsymbol{\varepsilon}}\boldsymbol{\varepsilon}^+ \in \mathcal{S}$ and $\partial_{\boldsymbol{\varepsilon}}\mathbf{A}\boldsymbol{\varepsilon}^- \in \mathcal{S}^*$, we have due to (14)

$$\boldsymbol{\sigma}_0^- \cdot \frac{\partial \boldsymbol{\varepsilon}^+}{\partial \boldsymbol{\varepsilon}}(\boldsymbol{\varepsilon})\mathbf{e} \leq 0 \text{ and } \boldsymbol{\sigma}_0^+ \cdot \frac{\partial \boldsymbol{\varepsilon}^-}{\partial \boldsymbol{\varepsilon}}(\boldsymbol{\varepsilon})\mathbf{e} \leq 0. \quad (17)$$

By differentiating the orthogonality condition (15) with respect to the total strain $\boldsymbol{\varepsilon}$, we find that the sum of the earlier two non-positive inner products equals to zero, which implies individually that these two expressions in (17) vanish. Recalling $\boldsymbol{\varepsilon} = \boldsymbol{\varepsilon}^+ + \boldsymbol{\varepsilon}^-$, the stress tensor is readily identified from (16)

$$\boldsymbol{\sigma}_t = \boldsymbol{\sigma}(\boldsymbol{\varepsilon}, \alpha) = a(\alpha)\boldsymbol{\sigma}_0^+ + \boldsymbol{\sigma}_0^-. \quad (18)$$

This is the stress expression $\boldsymbol{\sigma}_t$ that will be used in the weak elastodynamic equation (9) when tension–compression asymmetry is considered. It can be noted that this expression is reduced to its negative part $\boldsymbol{\sigma}(\boldsymbol{\varepsilon}, 1) = \boldsymbol{\sigma}_0^- \in \mathcal{S}^*$ for a totally damaged element.

Using this variational formulation (13), the modeling of material tension–compression asymmetry is thus reduced to the setting of such convex cone \mathcal{S} destined to represent the strains that contribute to damage. Several existing phase-field-like models of fracture can be derived within this framework [10].

- The original symmetric model of [18] can be trivially obtained by choosing \mathcal{S} to all symmetric second-order tensors. From (14), it can be deduced that $\boldsymbol{\varepsilon}^+ = \boldsymbol{\varepsilon}$, that is, the total strain contributes to damage irrespective of whether it corresponds to traction or compression.

- The deviatoric model of [9] is retrieved when \mathcal{S} represents all symmetric second-order tensors that have a zero trace (and the condition that \mathbf{A} is isotropic). Only the deviatoric part of the strain $\text{dev} \boldsymbol{\varepsilon}$ participates to damage. The negative stress $\boldsymbol{\sigma}_0^-$ belongs to the polar cone of \mathcal{S} , which is characterized by a zero deviatoric part. Thus, for a totally damaged material point, the stress is hydrostatic and has the form $p\mathbb{I}$ for $p \in \mathbb{R}$.
- The model of [21] is a combination of the previous two models. If the total strain corresponds to an expansion $\text{tr} \boldsymbol{\varepsilon} \geq 0$, the damage mechanism is completely active, and \mathcal{S} corresponds to all symmetric second-order tensors. However, if a compressive strain is present $\text{tr} \boldsymbol{\varepsilon} < 0$, only the deviatoric part of the strain $\text{dev} \boldsymbol{\varepsilon}$ participates to damage, and \mathcal{S} corresponds to all symmetric second-order tensors that have a zero trace. In this case, a totally damaged material point experiences a compressive hydrostatic pressure $p\mathbb{I}$ for $p \leq 0$.
- The masonry-like model of [10] is obtained when \mathcal{S} is chosen to include all positive semidefinite symmetric tensors. As \mathcal{S} is a convex cone, the stress tensor can be simplified to (18), and hence, the stress that can be attained by a totally damaged material point is necessarily negative semidefinite, corresponding in fact to materials that do not support tension [22]. However, the model as suggested by [10] with \mathcal{S} containing all symmetric tensors of which all eigenvalues are greater than -1 may present some difficulties, as the orthogonality condition (15) and the simplified stress expression (18) no longer apply and \mathcal{S} not being closed with respect to arbitrary positive rescaling.

It can be noted that the widely used tension–compression asymmetry model of [23] adopts the elastic energy density split (11) but does not fit into the variational formalism (13). Denoting $\boldsymbol{\varepsilon}^+$ (resp. $\boldsymbol{\varepsilon}^-$) as the positive (resp. negative) part of the total strain obtained by projecting $\boldsymbol{\varepsilon}$ onto the space of all symmetric positive (resp. negative) semidefinite tensors *with respect to the natural Frobenius norm*, their model reads

$$\begin{aligned}\psi_0^\pm(\boldsymbol{\varepsilon}) &= \frac{1}{2}\lambda\langle\text{tr} \boldsymbol{\varepsilon}\rangle_\pm^2 + \mu\boldsymbol{\varepsilon}_\pm \cdot \boldsymbol{\varepsilon}_\pm, \\ \boldsymbol{\sigma}_0^\pm(\boldsymbol{\varepsilon}) &= \lambda\langle\text{tr} \boldsymbol{\varepsilon}\rangle_\pm\mathbb{I} + 2\mu\boldsymbol{\varepsilon}_\pm\end{aligned}\quad (19)$$

where contrary to the formulation there is no more individual constitutive relation separately for the positive or the negative strain. Despite its variational inconsistency, the stress for a totally damaged element is also negative semidefinite as for the model of [10]. The qualitative differences between these two models will be illustrated in the following section.

3.2. Uniaxial traction and compression experiment

Here, we will investigate the theoretical behavior of the earlier outlined models under a very simple loading condition to illustrate their individual particularities. It can be understood that the underlying local damage model obtained by suppressing the gradient damage $\nabla\alpha_t$ in the dissipation energy density (3) represents the material behavior when no strain or damage localization appears. Hence, some general properties of these tension–compression asymmetry models can be extracted under an academic homogeneous three-dimensional uniaxial traction or compression experiment. Inertia is not essential for this analysis and will be neglected. We suppose that the stress tensor is of form $\boldsymbol{\sigma}_t = \sigma_{33}\mathbf{e}_3 \otimes \mathbf{e}_3$ corresponding to an imposed axial strain $\boldsymbol{\varepsilon}_{33} = t$ viewed as a loading parameter. Because \mathbf{A} is isotropic, the goal is to find the evolutions of the transversal strain $t \mapsto \boldsymbol{\varepsilon}_{11} = \boldsymbol{\varepsilon}_{22}$, the axial stress $t \mapsto \sigma_{33}$, and the homogeneous damage $t \mapsto \alpha_t$. This amounts to solve the following system when the damage evolves $\dot{\alpha}_t > 0$;

$$\sigma_{11}(t) = (a(\alpha_t)\boldsymbol{\sigma}_0^+ + \boldsymbol{\sigma}_0^-) \mathbf{e}_1 \cdot \mathbf{e}_1 = 0, \quad (20a)$$

$$\frac{\partial \psi}{\partial \alpha}(\boldsymbol{\varepsilon}_t, \alpha_t) + w'(\alpha_t) = 0 \quad (20b)$$

where $\boldsymbol{\varepsilon}_t = \boldsymbol{\varepsilon}_{11}(\mathbf{e}_1 \otimes \mathbf{e}_1 + \mathbf{e}_2 \otimes \mathbf{e}_2) + t\mathbf{e}_3 \otimes \mathbf{e}_3$. The second equation (20b) is the local interpretation of the energy balance condition (8) ([12]).

We remark that in order to solve (20), a particular set of damage constitutive laws also has to be chosen. Strictly speaking, the functions $\alpha \mapsto a(\alpha)$ and $\alpha \mapsto w(\alpha)$ should influence the exact behavior of the tension–compression asymmetry models. Nevertheless, we discover that the solutions obtained with two particular damage constitutive laws (PAMM) and (AT) share many qualitative properties.

The model of [21] has been already studied in this uniaxial traction and compression setting with the damage model (AT). The material undergoes a softening behavior both under tension or compression when a certain finite threshold σ_0^\pm is reached. The ratio between these two maximal stresses is given by

$$-\frac{\sigma_0^-}{\sigma_0^+} = \sqrt{\frac{3}{2(1+\nu)}} \leq \sqrt{\frac{3}{2}} \approx 1.22,$$

which is not sufficient for applications to brittle materials where this factor can attain 10. This ratio is the same when the damage constitutive law (PAMM) is used.

We then turn to the tension–compression separation proposed in [23]. Similar as it is to the model of [10] because both ones perform spectral decomposition of the total strain (with respect to two different inner products, although), their behavior under compression will be unexpectedly different. For the constitutive model of (PAMM), the material remains intact until a tensile σ_0^+ or a compressive σ_0^- stress threshold is reached

$$\sigma_0^+ = \sqrt{\frac{(1+\nu)}{(1-\nu)(1+2\nu)}} w_1 E,$$

$$\sigma_0^- = -\sqrt{\frac{1+\nu}{2\nu^2}} w_1 E \rightarrow \infty \text{ as } \nu \rightarrow 0.$$

It can be seen that the critical stress σ_0^+ increases with the Poisson ratio but stays bounded in tension. The compressive threshold σ_0^- goes to infinity when ν is near zero; hence, no damage will occur in this case. We use the tensile threshold σ_0^+ and its corresponding strain ϵ_0^+ both evaluated at $\nu = 0.2$ to normalize the results shown in Figure 2.

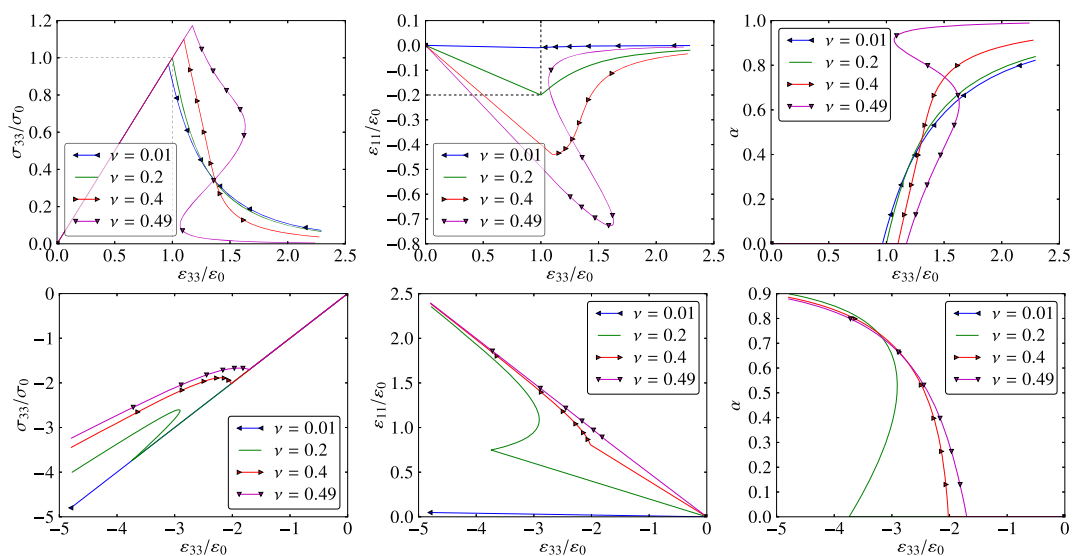


Figure 2. Uniaxial traction $\epsilon_{33} \geq 0$ and compression $\epsilon_{33} \leq 0$ experiments for the tension–compression asymmetry proposed in [23]. The damage constitutive law (PAMM) is used.

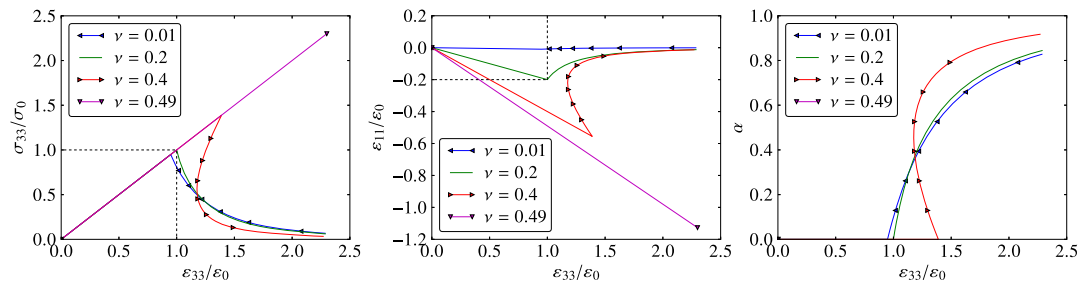


Figure 3. Uniaxial traction $\epsilon_{33} \geq 0$ experiment for the tension–compression asymmetry proposed in [10]. The damage constitutive law (PAMM) is used.

Remark that under a uniaxial tensile loading, the material undergoes a classical softening behavior when the threshold stress is reached. For quasi-incompressible materials $\nu \approx \frac{1}{2}$, a snapback is present, and hence, the evolution of the stress σ_{33} and the strain ϵ_{11} may experience a temporal discontinuity. However, this behavior is only limited to the law (PAMM), whereas for (AT), no snapback is observed. Unexpectedly, under compression, the material may experience a two-phase softening–hardening (with an initial snapback for $0 \leq \nu \leq 3/8$ limited to the (PAMM) case), while the damage increases. As α approaches 1, that is, as the material point becomes totally damaged, the uniaxial stress is not bounded and is given by $\sigma_{33} = 2\mu\epsilon_{33}$. Moreover, an apparent incompressible behavior is observed $\text{tr } \epsilon_t = 0$. These properties can be readily derived using the definitions (19). Because of a non-vanishing stress inside a completely damaged element, one may expect large diffusive ‘damage’ for highly compressive zones. This may complicate the physical interpretation of the model of [23] in this situation.

In contrast, for any damage constitutive laws, the model proposed in [10] does not permit any damage under uniaxial compression. The positive strain contributing to damage after projection (13) is given by $\epsilon^+ = (\epsilon_{11} + \nu\epsilon_{33})(\mathbf{e}_1 \otimes \mathbf{e}_1 + \mathbf{e}_2 \otimes \mathbf{e}_2)$, which vanishes because of the uniaxial stress state $\sigma_t = \sigma_{33}\mathbf{e}_3 \otimes \mathbf{e}_3$ implying $\epsilon_{11} = -\nu\epsilon_{33}$. Under traction and when using the damage law (PAMM), a stress threshold under which no damage appears is given by

$$\sigma_0^+ = \sqrt{\frac{(1-\nu)}{(1-2\nu)(1+\nu)}} w_1 E \rightarrow \infty \text{ as } \nu \rightarrow \frac{1}{2},$$

so cracks cannot appear for incompressible materials. We again use the tensile stress threshold σ_0^+ and its corresponding strain ϵ_0^+ both evaluated at $\nu = 0.2$ to normalize the results shown in Figure 3. A classical softening behavior is observed after damage initiation. Analyses show that snapbacks are present for $\nu > (\sqrt{33} - 1)/16 \approx 0.3$. However, it is only limited to the (PAMM) case.

3.3. How to choose among different models

Following the previous review and analyses of several existing models on tension–compression asymmetry, a natural question arises as to how to choose the best or the right one for a particular problem. If the variational formulation (13) is used, the problem can be reduced to choose a good convex cone \mathcal{S} of the second-order symmetric tensors. As the elastic energy density split (11) influences both the displacement and the damage problems through the first-order stability condition (7), these two aspects will be separately discussed.

- For the \mathbf{u} -problem, the tension–compression asymmetry model is widely recognized to approximate the material non-interpenetration condition [9, 21, 24]. However, we would like to recall that this approximation is merely heuristic. Taking into account, the actual non-interpenetration condition at finite strains in the sense of [25], that is, local orientation preservation and global injectivity, is a difficult task both from a theoretical or numerical point of view and, hence, is often merely checked *a posteriori*. Nevertheless, we could expect that the tension–compression

decomposition itself should depend on the local damage state and the damage gradient $\nabla\alpha_t$ approximating the local crack normal in the reference frame. A better elastic energy density split of (11) could be

$$\psi(\boldsymbol{\varepsilon}, \alpha, \nabla\alpha) = a(\alpha)\psi_0^+(\boldsymbol{\varepsilon}, \alpha, \nabla\alpha) + \psi_0^-(\boldsymbol{\varepsilon}, \alpha, \nabla\alpha). \quad (21)$$

When the crack is created, the elastic energy split itself should become orientation dependent so that only non-positive normal stress can be applied on crack lips if friction is not considered.

- For the α -problem, the decomposition (11) directly controls the type of strain or stress state, which initiates and produces further damage, deviatoric part in [9] or in [11] under compression and positive principal values in [10, 23]. We share the remark given in [24] that only experiments conducted with real materials can determine or identify a good model. We thus regard the elastic energy split (11) or the convex cone \mathcal{S} as another independent material property or parameter characterizing the microstructure. For rocks or stones, the deviatoric model may predict realistic crack path; however, for more brittle materials such as concrete or glass, models based on a spectral decomposition may be more suitable.

4. NUMERICAL IMPLEMENTATION

This section is devoted to the numerical implementation of Model 1 applied to explicit dynamic situations. The two damage constitutive laws (AT) and (PAMM) will be used. The elastic energy density split (11) is also adopted to take into account tension–compression asymmetry. Our implementation can be considered as an adaptation of the previous work of [1, 11, 26] on quasi-static and dynamic phase-field-like models for fracture. In this work, the irreversibility condition and the variational inequality (7) will be effectively implemented, which amounts to solve numerically the weak wave equation (9) and the minimality principle for damage (10) at every time step. However, it is shown in [27] that the time-discrete numerical model will also balance energy as required in (8), when the time increment becomes small. Their constructive proof makes use of the implicit Euler scheme used in [26]; however, our experience suggests the same for the explicit central difference scheme as we describe later.

In this contribution, the spatial and temporal discretizations are as usual decoupled and will be discussed later separately. Space-time finite element methods will exploit fully the variational nature of the formulation (7) and can be considered as a possible improvement in the future.

4.1. Spatial discretization

Classical finite element method is used to discretize in space the displacement \mathbf{u}_t and the damage field α_t based on a same mesh Ω_h . It should be ideally unstructured and uniform in mesh sizes; otherwise, some directions may be preferred when cracks propagate [11]. The typical element size h of the mesh should be preferably smaller with respect to the internal length ℓ in order to calculate correctly the damage band profile, the dissipation energy (3), and the material response inside the crack process zone of order $\mathcal{O}(\ell)$ ([6]).

4.1.0.1. Displacement problem. The displacement \mathbf{u}_t and the damage field α_t will be both discretized with linear isoparametric finite elements. Inside an arbitrary element $\Omega_e \in \Omega_h$, we thus have

$$\begin{aligned} \mathbf{u}_t(\mathbf{x}) &= \mathbf{N}(\mathbf{x})\underline{\mathbf{u}}^e \quad \text{and} \quad \boldsymbol{\varepsilon}(\mathbf{u}_t)(\mathbf{x}) = \mathbf{B}(\mathbf{x})\underline{\mathbf{u}}^e, \\ \alpha_t(\mathbf{x}) &= \mathbf{N}_\alpha(\mathbf{x})\underline{\alpha}^e \quad \text{and} \quad \nabla\alpha_t(\mathbf{x}) = \mathbf{B}_\alpha(\mathbf{x})\underline{\alpha}^e \end{aligned}$$

where \mathbf{N} 's and \mathbf{B} 's are respectively the interpolation and differentiation matrices applied on local nodal vectors $\underline{\mathbf{u}}^e$ and $\underline{\alpha}^e$ specific to the element Ω_e . Linear elements are used because of their low computational cost. According to [6], linear interpolations for the displacement and damage fields

perform equally well compared with higher-order elements in terms of Γ -convergence of the dissipation energy. Finally, this P1–P1 finite element discretization is not forbidden according to [28]. The weak form of the wave equation (9) after discretization in space reads

$$\mathbf{M}\ddot{\mathbf{u}} = \mathbf{F}_{\text{ext}} - \mathbf{F}_{\text{int}}(\mathbf{u}, \underline{\alpha}) \quad (22)$$

with \mathbf{M} the classical lumped mass matrix, \mathbf{F}_{ext} the external force vector corresponding to the potential (5), and \mathbf{F}_{int} the internal force vector assembled from the elementary vectors given by

$$\begin{aligned} \mathbf{F}_{\text{int}}^e &= \int_{\Omega_e} \mathbf{B}^T \boldsymbol{\sigma}(\mathbf{B}\mathbf{u}^e, \mathbf{N}_\alpha \underline{\alpha}^e) \, \mathrm{d}\mathbf{x} \\ &= \int_{\Omega_e} \mathbf{B}^T (a(\mathbf{N}_\alpha \underline{\alpha}^e) \boldsymbol{\sigma}_0^+(\mathbf{B}\mathbf{u}^e) + \boldsymbol{\sigma}_0^-(\mathbf{B}\mathbf{u}^e)) \, \mathrm{d}\mathbf{x}. \end{aligned} \quad (23)$$

We note here that in explicit dynamics, a residual stiffness k_{res} is not needed in the stiffness degradation function because no matrix inversion is needed, contrary to the implicit cases [3, 11].

4.1.0.2. Damage problem. Using the damage constitutive laws (AT) and (PAMM), the total damageable energy $\mathcal{E} + \mathcal{S}$ is quadratic with respect to the damage vector $\underline{\alpha}$ and (10) after spatial discretization reads

$$q_{\mathbf{u}}(\underline{\alpha}) \leq q_{\mathbf{u}}(\underline{\beta}) \text{ for all } \underline{\beta} \text{ that } 0 \leq \underline{\alpha} \leq \underline{\beta} \leq 1 \quad (24)$$

with the quadratic functional defined by

$$q_{\mathbf{u}}(\underline{\alpha}) = \frac{1}{2} \underline{\alpha}^T \mathbf{H}(\mathbf{u}) \underline{\alpha} - \mathbf{b}(\mathbf{u})^T \underline{\alpha}. \quad (25)$$

The Hessian matrix \mathbf{H} and the second member vector \mathbf{b} depend solely on the current deformation state \mathbf{u} and, hence, are constant during the solving process of the damage problem. Their exact forms depend on the damage constitutive law used. For the (PAMM) law for instance, they can be assembled from the elementary matrix and vector given by

$$\begin{aligned} \mathbf{H}^e &= \int_{\Omega_e} (2\psi_0^+(\mathbf{B}\mathbf{u}^e) \mathbf{N}_\alpha^T \mathbf{N}_\alpha + 2w_1 \ell^2 \mathbf{B}_\alpha^T \mathbf{B}_\alpha) \, \mathrm{d}\mathbf{x}, \\ \mathbf{b}^e &= \int_{\Omega_e} (2\psi_0^+(\mathbf{B}\mathbf{u}^e) - w_1) \mathbf{N}_\alpha \, \mathrm{d}\mathbf{x}. \end{aligned}$$

4.2. Temporal discretization

Given an arbitrary discretization (t^n) of the time interval of interest I where the superscript n denotes a quantity evaluated at the n th time step, our objective here is to solve the spatially discretized wave equation (22) coupled with the crack minimality condition (24) at these steps. In this contribution, we consider dynamic fracture problems in brittle materials under impact-type loadings. In general, the time scale involved is typically of order $\mathcal{O}(1\text{ms}) \ll \mathcal{O}(1\text{s})$; thus, in absence of a costly matrix inversion, the explicit Newmark scheme with a lumped mass matrix is very suitable for this kind of situations. This time-stepping method is known to be conditionally stable. After spatial discretization, the constraint prescribed on the current time increment Δt is often determined by the Courant–Friedrichs–Lewy (CFL) condition $\Delta t < \Delta t_{\text{CFL}} = \min(h/c)$ where h is the mesh size, c is the material sound speed, and the smallest value is chosen among all elements. In the calculation of the material sound speed, current damage state and the tension–compression split formulation are taken into account. Thus, a totally damaged element under tension does not penalize the total computational time.

We note that after temporal discretization (24) reads,

$$q_{\mathbf{u}^n}(\underline{\alpha}^n) \leq q_{\mathbf{u}^n}(\underline{\beta}) \text{ for all } \underline{\beta} \text{ that } 0 \leq \underline{\alpha}^{n-1} \leq \underline{\beta} \leq 1 \quad (26)$$

where the Hessian matrix and the second member vector in (25) are evaluated at $\underline{\mathbf{u}}^n$. It can be translated to an effective minimization of the quadratic functional q under the constraint that the current sought damage state $\underline{\alpha}^n$ is pointwise non-decreasing with respect to its previous value. In absence of the temporal derivative of the damage field $\dot{\alpha}_t$, the earlier equation (26) is not a genuine time evolution problem as the sole time dependence is introduced via the irreversibility condition. The current damage $\underline{\alpha}^n$ can be accurately calculated as long as the current deformation state $\underline{\mathbf{u}}^n$ is known.

In the time-continuous model, the wave equation (9) and the damage minimality condition (10) are coupled in the first-order stability principle (7). After temporal discretization, $\underline{\mathbf{u}}$ and $\underline{\alpha}$ evaluated at the last and current iterations are in general involved in an implicit fashion. In our case, it turns out that the explicit Newmark scheme automatically decouples the time evolution system in $(\underline{\mathbf{u}}, \underline{\alpha})$, and the two subproblems separately on $\underline{\mathbf{u}}$ and on $\underline{\alpha}$ can be independently solved one from the other at every time step. It is because the current acceleration $\ddot{\underline{\mathbf{u}}}^n$ can be obtained based on the current known deformation state $\underline{\mathbf{u}}^n$ and the current damage $\underline{\alpha}^n$ calculated from $\underline{\mathbf{u}}^n$. The time-stepping scheme can be summarized in Algorithm 1. A bound-constrained minimization problem appears in every time iteration of the elastodynamic equation, and thus, its efficient implementation is crucial. We observe that the initial damage is recomputed $\underline{\alpha}^{-1} \mapsto \underline{\alpha}^0$ in the step 2. The role of $\underline{\alpha}^{-1}$ is to bring some *a priori* knowledge of the damage field resulting from a previous calculation or more frequently to represent an initial crack $\underline{\alpha}^{-1} = 1$ on Γ_0 . The initial step 2 thus renders it compatible with the initial displacement condition and the energy minimization structure.

Algorithm 1 Discretized numerical model of Model 1.

- 1: Given initial conditions $\underline{\mathbf{u}}^0, \dot{\underline{\mathbf{u}}}^0$ and $\underline{\alpha}^{-1}$.
 - 2: Reinitialize the damage $\underline{\alpha}^0 = \operatorname{argmin} q_{\underline{\mathbf{u}}^0}(\cdot)$ subjected to constraints $0 \leq \underline{\alpha}^{-1} \leq \underline{\alpha}^0 \leq 1$.
 - 3: Initialize the acceleration $\mathbf{M}\ddot{\underline{\mathbf{u}}}^0 = \mathbf{F}_{\text{ext}}^0 - \mathbf{F}_{\text{int}}(\underline{\mathbf{u}}^0, \underline{\alpha}^0)$.
 - 4: **for** every successive time step $n \geq 0$ **do**
 - 5: Update $\dot{\underline{\mathbf{u}}}^{n+1/2} = \dot{\underline{\mathbf{u}}}^n + \frac{\Delta t}{2} \ddot{\underline{\mathbf{u}}}^n$.
 - 6: Update $\underline{\mathbf{u}}^{n+1} = \underline{\mathbf{u}}^n + \Delta t \dot{\underline{\mathbf{u}}}^{n+1/2}$.
 - 7: Update $\underline{\alpha}^{n+1} = \operatorname{argmin} q_{\underline{\mathbf{u}}^{n+1}}(\cdot)$ subjected to constraints $0 \leq \underline{\alpha}^n \leq \underline{\alpha}^{n+1} \leq 1$.
 - 8: Update $\mathbf{M}\ddot{\underline{\mathbf{u}}}^{n+1} = \mathbf{F}_{\text{ext}}^{n+1} - \mathbf{F}_{\text{int}}(\underline{\mathbf{u}}^{n+1}, \underline{\alpha}^{n+1})$.
 - 9: Update $\dot{\underline{\mathbf{u}}}^{n+1} = \dot{\underline{\mathbf{u}}}^{n+1/2} + \frac{\Delta t}{2} \ddot{\underline{\mathbf{u}}}^{n+1}$.
 - 10: **end for**
-

4.3. Implementation

Contrary to a pure explicit dynamic calculation, the presence of an implicit damage problem (26) calls for a parallel linear algebra backend for manipulation of sparse matrices and vectors. As in the work of [16], the library PETSc [29] is adopted because it provides also an efficient numerical scheme Gradient Projection Conjugate Gradient (GPCG) initially proposed in [30], designed for quadratic bound-constrained minimization problems. It consists of several gradient projections to identify the active nodes, that is, those either $\underline{\alpha}^n = \underline{\alpha}^{n-1}$ or $\underline{\alpha}^n = 1$. Then, it applies the preconditioned conjugate gradient (PCG) method to minimize an unconstrained reduced problem of the free variables, that is, those satisfying $\underline{\alpha}^{n-1} < \underline{\alpha}^n < 1$. The incomplete Cholesky factorization preconditioner is applied block-wise onto each decomposed subdomain. Our simulation results demonstrate that this scheme is robust and efficient. Computational load is also well balanced [31] in parallel computations based on domain decomposition.

Algorithm 1 has been fully implemented in EUROPLEXUS, an explicit dynamics program dedicated to transient phenomena involving fluid-structure interaction [32]. Meanwhile, an open-source implementation of the model is also available [33]. It is based on the FEniCS Project [34] for automated solution of partial differential equations.

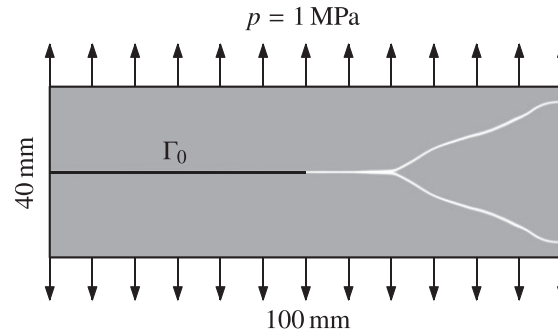


Figure 4. Geometry and loading conditions for the dynamic crack branching problem. Damage field α_t at $t = 8 \times 10^{-5}$ s ranging from 0 (gray) to 1 (white).

5. SIMULATION RESULTS

5.1. Dynamic crack branching

We will first study the dynamic crack branching problem for a two-dimensional plane stress plate under constant pressure applied on its upper and lower boundaries. This particular problem has already been investigated within the phase-field community [1, 3] where the numerical convergence aspect and the physical insight into the branching mechanism are analyzed. Here, we will mainly focus on the computational efficiency and the possible use of several damage constitutive laws to approximate fracture.

The geometry and the loading conditions are depicted in Figure 4. Due to symmetry only, the upper half part is modeled. The initial crack Γ_0 is introduced via an initial damage field α^{-1} . Material parameters are borrowed from [1] where the internal length ℓ is set to 0.25 mm. We use a structured quadrilateral elements of equal discretization spacing $h \approx 0.045$ mm in both directions achieving approximately 1 million elements. The current time increment is calculated based on the Courant-Friedrichs-Lewy (CFL) condition with a security factor of 0.8. An unstructured mesh should be in general preferred. However, the original analysis on mesh-induced anisotropy is conducted on structured triangular elements [35]. Furthermore, the numerical study of [36] shows that the crack direction is insensitive to the orientation of a structured quadrilateral grids. We firstly use the damage constitutive law (PAMM). The symmetric tension-compression formulation is also adopted. This choice is justified by an *a posteriori* verification of non-interpenetration of matter. The simulation result is illustrated in Figure 4 by the damage field α_t at $t = 8 \times 10^{-5}$ s ranging from 0 (gray) to 1 (white). Similar contours have been obtained in [1, 3].

A strong scaling analysis is conducted by varying the number of processor cores NP in the cluster Aster5 provided by the Electricité de France. We have verified that all simulations give nearly the same results in terms of global energy evolution and field contours. The difference of the elastic energy at $t = 8 \times 10^{-5}$ s is within 0.2% between the sequential and the parallel NP = 16 cases, which may be due to floating point arithmetic and different setting of preconditioners. The scaling results are given in Figure 5. The calculation time is partitioned into four items: the ‘elastodynamics’ part related to the solving of (22), the ‘damage assembly’ part where the global Hessian matrix \mathbf{H} and the second member \mathbf{b} are constructed, the ‘damage solving’ part where (26) is solved, and the ‘communication’ part corresponding to the data exchange among processors. The maximum value among all processors are used. Quasi-ideal scaling is observed for the total computational time. The proportion of the ‘elastodynamics’ and the ‘damage assembly’ parts are decreasing, because of the increase of the ‘communication’ overhead reaching 15% with 16 cores and becoming comparable with that of the ‘damage solving’.

We remark that the quadratic bound-constrained minimization problem (26) solved by the GPCG scheme implemented in PETSc is not very costly and represents in sequential and parallel calculations only 13% of the total computational time. In the phase-field literature, the damage problem is often solved by an unconstrained minimization of (26) corresponding to a linear system

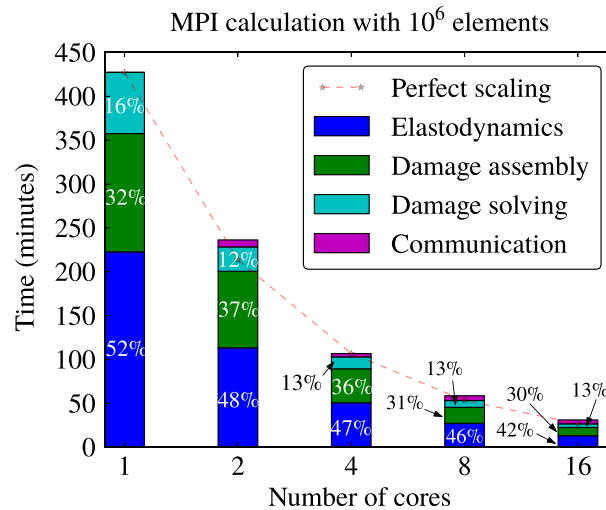


Figure 5. Strong scaling results for the dynamic crack branching problem with 1 million elements.

Table I. Relative damage-solving cost normalized by the time devoted to the elastodynamic part during a parallel calculation $NP = 16$.

	CG + projection	GPCG
Damage-solving cost	50%	77%

The damage constitutive law (AT) is used. Comparison between the GPCG solver and the *a posteriori* projection method.

$$\mathbf{H}\underline{\alpha} = \mathbf{b}. \quad (27)$$

To reinforce irreversibility, either the damage driving term is replaced by a history field [1, 2], or (27) is followed by an *a posteriori* projection in the admissible space ([9]). However, it should be kept in mind that the earlier computationally-appealing strategy only applies to the damage constitutive law (AT), where the solution of (27) lies necessarily between 0 and 1 and the objective functional q is indeed quadratic with respect to $\underline{\alpha}$. Otherwise, a specific numerical scheme for bound-constrained problems is needed. Nevertheless, we would like to point out that the GPCG solver is extremely efficient even compared with the earlier strategy consisting of only one linear equation. The same crack branching analysis is conducted using the damage constitutive model (AT) and a same internal length $\ell = 0.25$ mm, and the results obtained with the GPCG solver and the earlier *a posteriori* projection method are compared. In the latter case, the same PCG method is employed to solve (27). The results are slightly different as expected, because the projection method does not solve exactly the full minimization problem (26). To compare their relative computational costs, the time consumed in damage solving is separately normalized by that corresponding to the elastodynamic problem in Table I. Opposed to what is suggested by [21], the use of a bound-constrained minimization solver implies a relative computational cost only 27% higher than a traditional linear solver. This can be seen in the normalized histogram of CG iterations per time step illustrated in Figure 6. We recall that each CG iteration implies a matrix-vector multiplication, the most costly part of the algorithm. When only one linear system is to be solved in the *a posteriori* projection method, approximately 20 CG iterations are needed in 35% of all time steps. When the GPCG solver is used, we observe that the histogram is more spread out and more than 50 CG iterations may be needed for some time steps. Nevertheless, the distribution is more concentrated around 10–30 iterations.

We then turn to the choice of different damage constitutive laws from a computational and physical point of view. We take the simulation results using (PAMM) as a reference and compare it with the widely used damage constitutive law (AT) in the phase-field modeling of fracture.

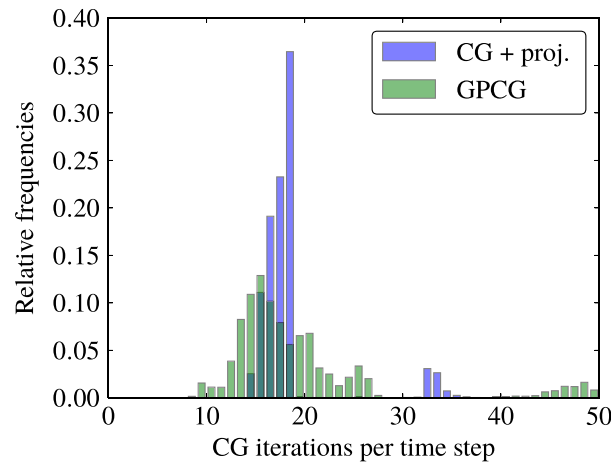


Figure 6. Normalized histogram of CG iterations per time step. The damage constitutive law (AT) is used. Comparison between the GPCG solver and the *a posteriori* projection method.

Table II. Relative damage-solving cost normalized by the time devoted to the elastodynamic part during a parallel calculation $NP = 16$.

Damage-solving cost	
(PAMM)	32%
(AT) with a same ℓ	77%
(AT) with a same σ_m	36%

The GPCG solver is used. Comparison between different constitutive laws.

The quantitative effects of the internal length actually depend on the damage constitutive model used. Here, we propose two natural choices of ℓ in the (AT) case: one corresponding to the same value $\ell = 0.25$ mm as used in the (PAMM) case and the other corresponding to a same maximal tensile stress as used in the (PAMM) case, which gives $\ell \approx 0.07$ mm. We recall from [11] that the maximal stress that can be supported by a gradient damage material is given by

$$\sigma_m = \begin{cases} \sqrt{\frac{3G_c E}{8\ell}} & \text{(PAMM) case,} \\ \frac{3\sqrt{3}}{16} \sqrt{\frac{G_c E}{\ell}} & \text{(AT) case,} \end{cases} \quad (28)$$

which determines the internal length as long as the material toughness and the Young's modulus are fixed. The same GPCG solver is used and the relative damage-solving costs separately normalized by the time devoted to the elastodynamic part are reported in Table II. We remark that the use of the constitutive law (PAMM) or a smaller internal length ℓ reduces significantly the relative damage-solving cost. A viable explanation is given as follows. The theoretical one-dimensional damage profile of (AT) corresponds to an exponential function without a finite support [6, 23]. The damage band $2D$, that is, in which $\alpha_t > 0$, is much wider than the (PAMM) case where $D = 2\ell$. Consequently, less active nodes are present, and the GPCG solver identifies much more free nodes for the (AT) case, which induces a bigger linear system to be solved. Similarly, a reduction of the material internal length may imply finer mesh along the crack path; however, the damage is more concentrated, and the relative solving cost is decreased.

The damage field α_t at $t = 8 \times 10^{-5}$ s obtained with the constitutive law (AT) is illustrated in Figure 7. Recall that the same mesh with $h = 0.05$ mm is used and should be sufficient for both calculations. Compared with Figure 4 obtained with (PAMM), the transition area where $0 < \alpha_t < 1$ is more pronounced especially in Figure 7 with $\ell = 0.25$ mm, conforming to the earlier discussions

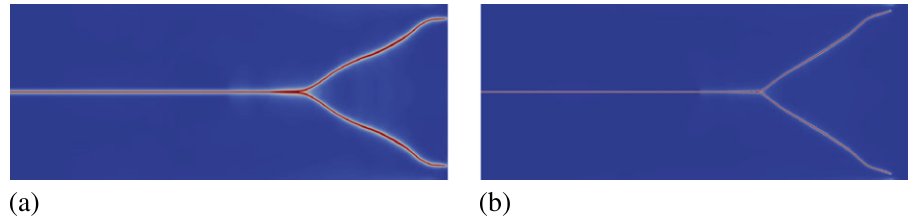


Figure 7. Damage field α_t at $t = 8 \times 10^{-5}$ s ranging from 0 (blue) to 1 (red) for the dynamic branching problem. Comparison between (a) $\ell = 0.25$ mm and (b) $\ell \approx 0.07$ mm with the same constitutive model (AT).

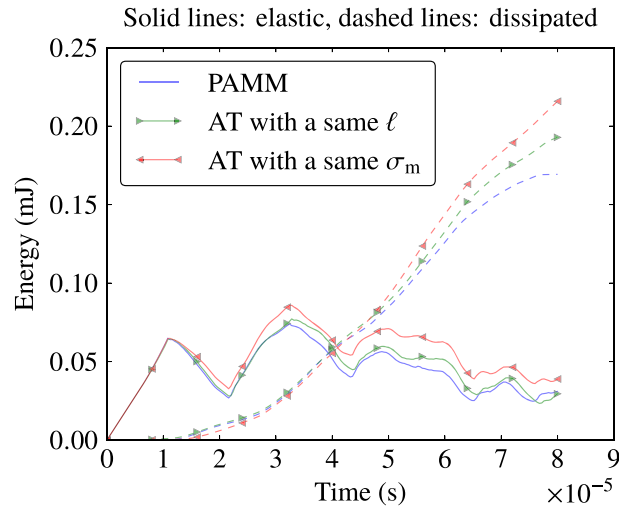


Figure 8. Energy evolution for the dynamic crack branching problem obtained with several constitutive laws.

on the damage band. Another reason behind a relatively large zone with intermediate damage values is due to the different stress–strain behavior of these two constitutive laws during a homogeneous traction experiment [11]. In the (PAMM) case, the material possesses a purely elastic domain and damage does not evolve as long as the maximal stress in (28) is not reached. Then, the material follows a classical softening behavior as damage grows from 0 to 1. However, for the constitutive law (AT) widely used in phase-field modeling, damage evolves the instant when the material is subjected to external loadings. An elastic domain is absent, and stress hardening is observed within the damage interval $[0, \frac{1}{4}]$, as is already been reported by [1, 3]. In this case, the phase-field α_t loses its physical interpretation as damage, and hence, correctly handling and interpreting crack healing are not trivial [3].

Furthermore, this peculiar behavior of the constitutive law (AT) also contributes to an overestimation of the dissipated energy, as is noted in [1, 37]. The energy evolution in this dynamic crack branching problem is given in Figure 8. It is observed that the (AT) law produces a dissipated energy much bigger than the (PAMM) case, although according to Figure 7, the damage fields are similar.

As can be seen from Figures 7 and 8, apparently, the results obtained with the same internal length ℓ resembles better the (PAMM) calculation in Figure 4, even though it corresponds to a smaller maximal stress than the latter case. It should be reminded that ℓ does not play merely the role of determination of the maximal stress as in (28). From [12], this parameter also contributes qualitatively to the separation of the outer linear elastic fracture mechanics problem and the inner crack tip problem in an asymptotic context. A smaller internal length implies a wider region outside the crack where the fracture mechanics theory may apply. Meanwhile, a size effect is also introduced via this internal length as it influences the stability of a structure [38]. We admit that the choice of this parameter is not a simple one and may constitute one of the difficulties in phase-field modeling of fracture problems.

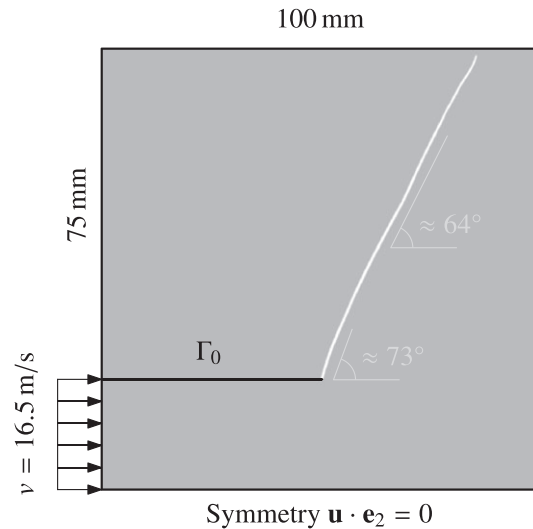


Figure 9. Geometry and boundary conditions for the edge-cracked plate under shearing impact problem. Damage field α_t at $t = 8 \times 10^{-5}$ s ranging from 0 (gray) to 1 (white).

5.2. Edge-cracked plate under shearing impact

We then consider a pre-notched two-dimensional plane strain plate impacted by a projectile. In the dynamic fracture community, this is often referred as the Kalthoff–Winkler experiment reported by, for example, [39] where a failure mode transition from brittle to ductile fracture is observed for a high-strength maraging steel when the impact velocity is increased. Due to symmetry, only the upper half part of the plate will be considered. The geometry and the boundary conditions for the reduced problem are described in Figure 9.

As in [1, 2], the projectile impact is modeled by a prescribed velocity with an initial rise time of 1×10^{-6} s to avoid acceleration shocks. The material parameters are borrowed from [1] except that the internal length ℓ is set to 0.2 mm. An unstructured and uniform triangular mesh with $h \approx 0.1$ mm is used, arriving at approximately three million elements. The current time increment is again calculated based on the CFL condition with a security factor of 0.8. Because of a lower computational cost and a more brittle material behavior, the damage constitutive law (PAMM) is used for this simulation.

As a reference, we use the elastic energy split proposed in [10] where the positive semidefinite part of the total strain will contribute to damage. The initial crack is introduced via a real notch in the geometry. A similar strong scaling curve as Figure 5 is obtained with up to 32 cores. Because of the additional spectral decomposition, the ‘damage assembly’ phase represents now approximately 50% of the total computational time, while the ‘damage solving’ still accounts for only 10%. The actual computation of the eigenvalues and eigenvectors of a 3×3 symmetric matrix is performed by a robust and efficient semi-analytic algorithm described in [40]. The damage field α_t at $t = 8 \times 10^{-5}$ s is depicted in Figure 9, obtained with an imposed impact speed $v = 16.5$ m/s. The initial and average propagation angles are in good agreement with the experimental results and other phase-field simulations [1, 2] based on the damage constitutive law (AT) and the tension–compression asymmetry formulation proposed by [23].

If the initial crack Γ_0 is modeled via an initial damage field α^{-1} , as for the previous dynamic crack branching example, no crack propagation is observed and the structures behaves as if the crack does not exist, *i.e.* the crack closure phenomenon. The horizontal displacement u_x obtained in both cases at $t \approx 2.4 \times 10^{-5}$ s when the real notch case starts to propagate is presented in Figure 10.

In the real notch-induced initial crack case, *contact condition is not prescribed* on the initial crack lips distanced by a finite height $\approx h$ in the geometry. As can be checked from Figure 10, no material interpenetration happens in the real notch case, and waves propagate in the plate through the lower impacted edge. However, in the damage-induced initial crack case, possible normal compressive

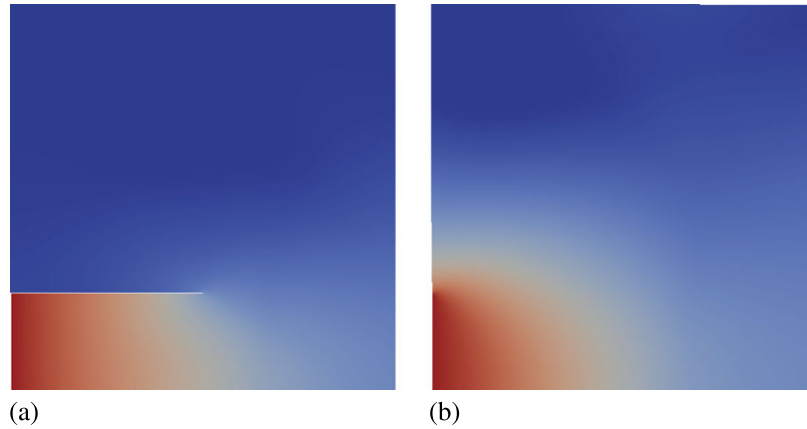


Figure 10. Displacement u_x ranging from 0 mm (blue) to 0.4 mm (red) for (a) the real notch-induced initial crack and (b) the damage induced initial crack, at $t \approx 2.4 \times 10^{-5}$ s when the crack starts to propagate in the real notch case (a).

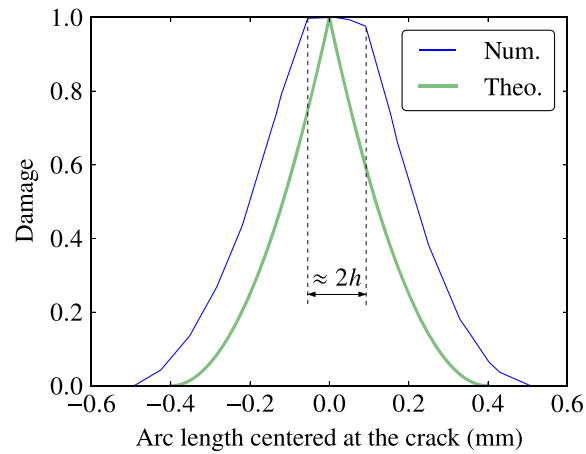


Figure 11. Damage profile perpendicular to the crack.

stresses can indeed be transferred to the upper part of the plate, via the tension–compression asymmetry model [10], which simulates a crack closure. Nevertheless, our simulation illustrates that this model also prohibits tangential relative movement along the crack lips, and a perfect adhesion (no-slip condition) is observed, that is, exactly the opposite situation compared with the real notch case. This result is expected from our discussions on future improvement of these tension–compression formulations in Section 3.3. The failure of these elastic energy decompositions to account for the actual damage value or its gradient approximating the crack normal has been reported by [41]. In the subsequent discussions, we will only consider the case where the initial crack is introduced via a real notch in the geometry.

The numerically obtained damage profile on a cross-section in the reference configuration parallel to the crack normal is compared with the theoretical one given by $\alpha(x) = (1 - |x|/D)^2$ with $D = 2\ell$ in the (PAMM) case [11]. From Figure 11, it can be observed that the numerical damage profile is wider than the analytical prediction by approximately $2h = 0.2$ mm. This phenomena leads to the definition of a numerically amplified effective fracture toughness $(G_c)_{\text{eff}}$, see [6], which in this example is given by $(G_c)_{\text{eff}} = (1 + 3(2h)/(8\ell)) G_c$ corresponding to the constitutive law (PAMM) adapted from [42].

From the Γ -convergence result [6], the crack length l_t can be estimated by

$$\mathcal{S}(\alpha_t) \approx (G_c)_{\text{eff}} \cdot l_t. \quad (29)$$

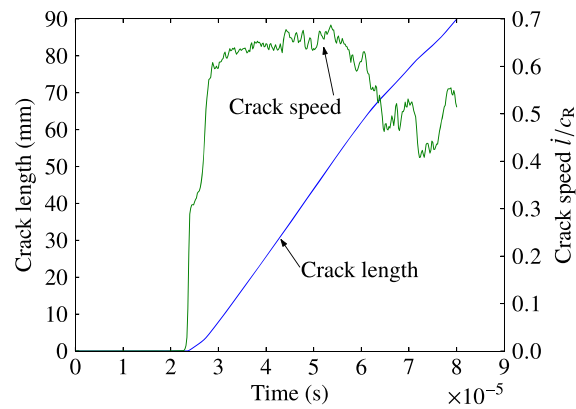


Figure 12. Crack length and velocity obtained for the edge-cracked plate with an imposed impact speed $v = 16.5 \text{ m/s}$.

A second-order difference scheme is then used to calculate the crack velocity.

As can be seen from Figure 12, the crack speed is well bounded by the Rayleigh wave speed (here $0.7c_R$), the theoretical limiting speed for an in-plane crack. It should be noted that this upper bound is rooted in the stability condition (7) and the energy balance (8), contrary to the thick level set approach [43] where this limiting speed is considered as an additional modeling parameter. The crack length is approximately 90 mm at $t = 8 \times 10^{-5} \text{ s}$ when the crack is about to reach the boundary (cf. Figure 9). This estimation agrees fairly well with a direct calculation based on a straight crack propagating at 64° , which gives about 83 mm. We believe that the discrepancy on crack length and a smaller limiting speed for brittle materials reported in experiments can be attributed to the dynamic instability mechanism reviewed in [44]. As the crack speed approaches a critical speed approximately $0.4c_R$, micro-branches appear along the main crack, and hence, more energy is dissipated during propagation. In that case, (29) is no longer valid and the apparent fracture toughness should be adapted to be velocity dependent. With the (AT) constitutive law, authors of [1, 37] report a systematic overestimation of the damage dissipation energy according to (29). Following our discussion in the previous simulation, we suspect that it is mainly due to the absence of a purely elastic domain and because damage evolves even in the stress-hardening phase. However, in the definition of the fracture toughness, this phenomena is not taken into account [6].

When the prescribed impact velocity is increased from $v = 16.5 \text{ m/s}$ to $v = 100 \text{ m/s}$, successive crack branching and nucleation of cracks at the lower-right corner due to high tensile stresses are observed as can be seen from Figure 13. The hydrostatic stress $p_t = \frac{1}{2} \text{tr} \sigma_t$ is presented in the deformed configuration, and we verify that no damage is produced in the compression zones. To visualize the crack, elements with $\alpha_t > 0.9$ are hidden in the graphical output. Similar phenomena have been reported in [2] with $v = 50 \text{ m/s}$. Recall that in the Kalthoff–Winkler experiment, a failure-mode transition from modes I to II is observed when the impact velocity increases. The discrepancy between our simulation and the experiment is due to the material constitutive behavior. As a material parameter, the tension–compression formulation [10] coupled with a purely elastic model favors propagation of mode-I cracks in the direction perpendicular to the maximal principle stress. On the contrary, the high-strength steel used in the experiment develops a considerable plastic zone along the mode-II crack, and an elastic–plastic–damage model should be more suitable [5]. Nevertheless, experimentally more bifurcations are indeed observed for brittle materials such as glass when the impact velocity is increased, which is known as a velocity effect in [45].

On the other hand, the widely used elastic energy density split proposed in [23] produces diffusive damage in compression zones. From Figure 14, we observe appearance of damage at the lower-left corner and at the lower surface of the initial crack edge, even though they are both under compression. This phenomena is conforming to our previous theoretical analysis of this model on a homogeneous uniaxial compression experiment in Section 3.2, where it is found that damage grows even though the compressive stress is still increasing in its absolute value.

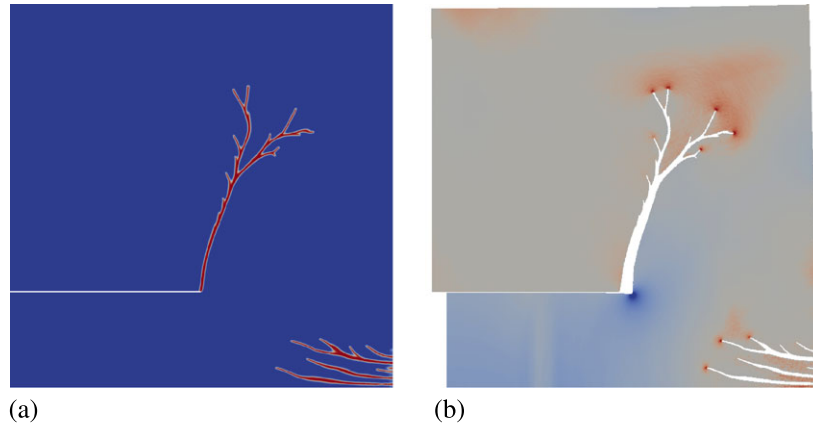


Figure 13. Simulation results at $t = 4 \times 10^{-5}$ s with an impact speed $v = 100$ m/s: (a) the damage field α_t ranging from 0 (blue) to 1 (red) and (b) the hydrostatic stress $\frac{1}{2} \text{tr } \sigma_t$ ranging from less than -1×10^4 MPa (blue) to more than 1.5×10^3 MPa (red). The tension–compression asymmetry model [10] is used.

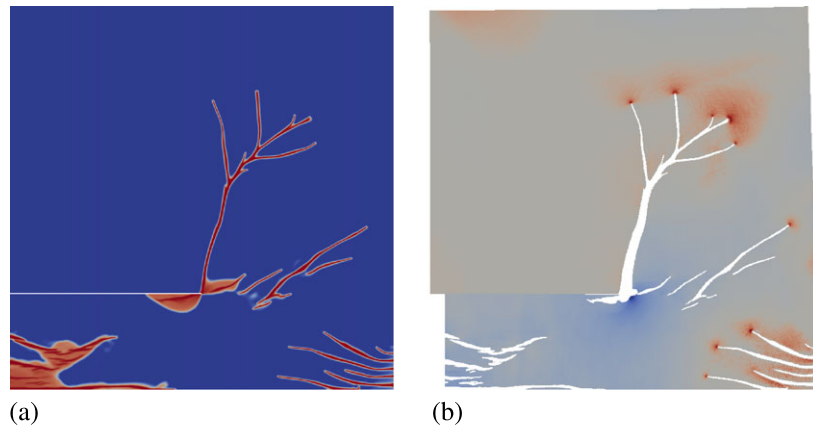


Figure 14. Simulation results at $t = 4 \times 10^{-5}$ s with an impact speed $v = 100$ m/s: (a) the damage field α_t ranging from 0 (blue) to 1 (red), and (b) the hydrostatic stress $\frac{1}{2} \text{tr } \sigma_t$ ranging from less than -1×10^4 MPa (blue) to more than 1.5×10^3 MPa (red). The tension–compression asymmetry model [23] is used.

The tension–compression split based on the trace of the total strain [21] is also tested. In [9], the pure compression version of this model is used to simulate shear cracking behavior in the stone ashlars. In this dynamic impact problem, we also observe at $t \approx 7 \times 10^{-6}$ s appearance of mode-II cracks originating from the impacted edge (Figure 15). We conclude that the tension–compression split (11) could indeed be considered as a material parameter as it represents the fracture mechanism determined by the microstructure. Note however that the calculation suddenly stops after that time due to an extremely small CFL time step $\Delta t_{\text{CFL}} = h/c$, which is caused by a highly distorted element $h \rightarrow 0$ in our updated Lagrangian formulation. The same numerical issue has been reported by [22] in which an Ogen hyperelastic model is used. Remark that the use of a tension–compression split based on the positive eigenvalues of the strain, that is, that of [10, 23], actually circumvents this problem by revising the material constitutive behavior.

5.3. Crack arrest due to the presence of a hole

Finally, we propose to experimentally validate the dynamic gradient damage model following the work of [8]. The problem considered is the ‘one crack two holes’ test studied in [46], where it is found that in dynamics cracks may be pushed away from the holes present in the domain due to wave reflections. The geometry and the boundary conditions are recalled in Figure 16.

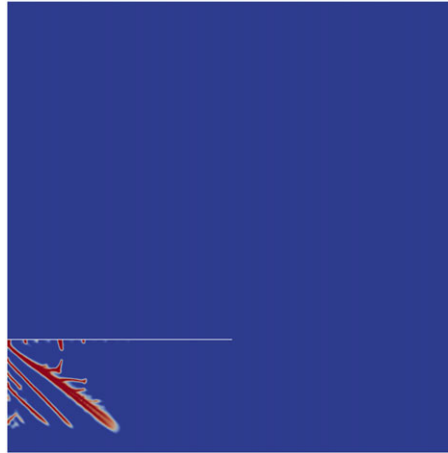


Figure 15. Damage field at $t \approx 7 \times 10^{-6}$ s obtained for the edge-cracked plate with an imposed impact speed $v = 100$ m/s. The elastic energy split [21] is used.

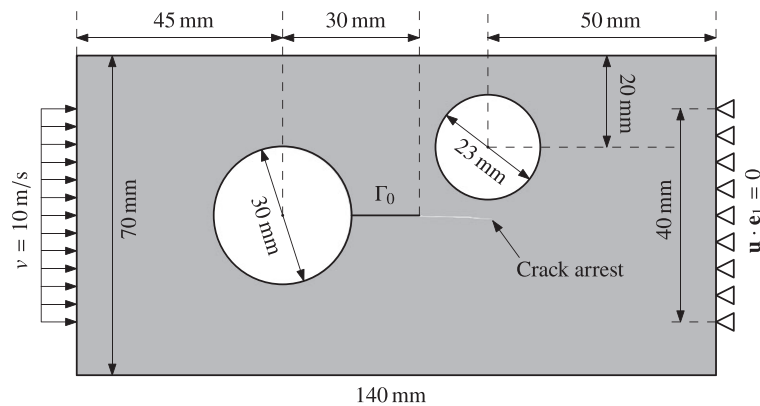


Figure 16. Geometry and boundary conditions for the ‘one crack two holes’ experiment studied in [46]. Damage field α_t at $t = 2 \times 10^{-4}$ s ranging from 0 (gray) to 1 (white).

Plane stress condition is assumed. Initial crack is introduced via a real notch in the geometry. The damage constitutive law (PAMM) is used again because of its interesting properties discussed in the dynamic crack branching problem. Because the material used (polymethylmethacrylate, or PMMA) is brittle [47] and the model of [23] possesses a peculiar behavior under high compression, the tension-compression asymmetry formulation proposed by [10] is adopted. Materials properties of PMMA, including the density, the dynamic Young’s modulus, and the Poisson ratio, are borrowed from [46]. In their calculations, crack propagation is based on a variant of the Griffith’s law where one critical stress intensity factor $K_{IC} = 1.03 \text{ MPa } \sqrt{\text{m}}$ predicts initiation and another $K_{IA} = 0.8 \text{ MPa } \sqrt{\text{m}}$ determines crack propagation and arrest. The latter one is used in our calculation as it deals with the most important phase of crack evolution. It is then converted to the fracture toughness

$$G_c = \frac{K_{IA}^2}{E} \approx 0.2667 \text{ N/mm} \quad (30)$$

thanks to the Irwin’s formula under plane-stress condition. The material internal length, or equivalently the maximal tensile stress of PMMA used in the experiment through (28), is unknown. Two reasonable values are tested corresponding respectively to a critical stress 70 MPa or 80 MPa, which gives along with (30) either $\ell \approx 0.05 \text{ mm}$ or $\ell \approx 0.0375 \text{ mm}$. An unconstrained mixed triangular-quadrilateral mesh refined with $h \approx 2 \times 10^{-2} \text{ mm}$ near the initial crack, and all possible nucleation

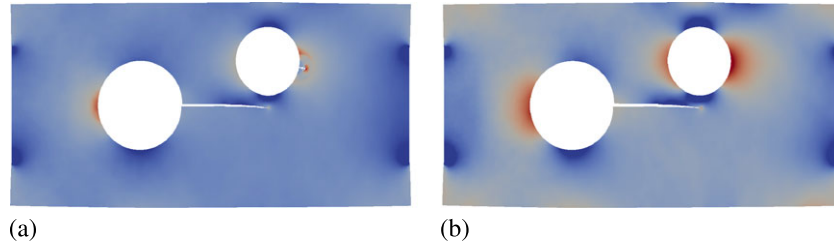


Figure 17. Hydrostatic stress $p_t = \frac{1}{2} \text{tr} \sigma_t$ ranging from less than -30 MPa (blue) to more than 30 MPa (red) for (a) $\sigma_m = 70$ MPa at $t \approx 1.6 \times 10^{-4}$ s and (b) $\sigma_m = 80$ MPa at $t \approx 1.8 \times 10^{-4}$ s in the crack arrest problem.

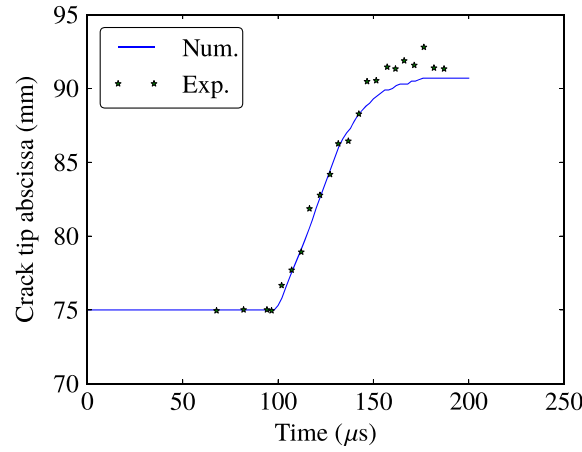


Figure 18. Crack tip abscissa evolution in the crack arrest problem. Comparison between the $\sigma_m = 80$ MPa case and the experimental results.

sites is used, arriving at approximately 400 000 elements. The current time increment is updated based on the CFL condition with a security factor of 0.8.

The simulations results are illustrated in Figure 17. In both cases, crack arrest is reproduced because of the high-compression area under the right circular hole. In the case when the maximal tensile stress is set to $\sigma_m = 70$ MPa, secondary crack nucleation is observed at the right circular hole boundary under high tension. This phenomena is not observed in experiments, and hence, the critical stress value of $\sigma_m = 70$ MPa is thus underestimated. In the $\sigma_m = 80$ MPa case, no secondary crack nucleation is found. This result again highlights the role played by the internal length ℓ as a material parameter.

As the crack front is not explicitly tracked in phase-field modeling of fracture, here, the current crack tip is located on the contour $\alpha = 0.9$ at the farthest point in the x -direction. We then compare the numerical crack tip abscissa evolution with the experimental one [46], in Figure 18. Very good agreement can be found in the crack initiation and propagation phase. The crack arrest predicted is slightly conservative compared with the experimental one. This could be due to the small deviation of the initial crack from the symmetry axis in the experiment [46]. Meanwhile the maximal tensile stress $\sigma_m \geq 80$ MPa could be considered as an adjusting parameter of the model. More simulations could be performed to determine its best value, at a price of using a more refined mesh because $\ell \propto 1/\sigma_m^2$ according to (28).

6. CONCLUSION

In this paper, a variationally consistent dynamic gradient damage model is proposed. Its use as a phase-field model of dynamic fracture problems is studied. It could be computationally more

demanding compared with traditional approaches based on a sharp description of cracks. The Griffith's law combined with specialized numerical methods could perform reasonably well with much less computational cost for fracture problems in absence of crack nucleation and complex topology changes. The major advantage of phase-field modeling reside in its generality in treating two-dimensional and three-dimensional crack evolution problems by providing a unified framework from onset to structural failure. Thanks to an efficient parallelization of the solving algorithm, the computing time can also be significantly reduced as demonstrated in Figure 5.

Two particular damage constitutive laws (AT) and (PAMM) are compared both from a computational and physical points of view. On one hand, the widely used crack surface density function (AT) is less suitable to model brittle fracture because an elastic domain is absent. On the other hand, the actual solving of the damage minimization problem (26) is more costly than the damage constitutive law (PAMM), which possesses an optimal damage profile of finite band. It is also illustrated that the cost of a general quadratic bound-constrained minimization solver is acceptable.

Different tension–compression asymmetry formulations in Section 3 are also tested. Some physical properties derived through a uniaxial traction experiment are verified in actual dynamic fracture problems. The elastic energy split proposed in [10] is recommended for brittle materials because homogeneous (diffusive) damage does not occur under compression. However, these models should be modified to correctly account for the unilateral contact condition. A better strategy may be to use a transition algorithm between the phase-field and the sharp-interface descriptions of cracks.

We conclude that the gradient damage model and its current implementation could indeed be used to approximate and investigate real dynamic brittle fracture problems with sufficient computational efficiency. Future work will be devoted to experimental validation of the model in three-dimensional cases and a better understanding of the first-order stability condition (7) in case of micro and macro-branching phenomena.

REFERENCES

1. Borden MJ, Verhoosel CV, Scott MA, Hughes TJR, Landis CM. A phase-field description of dynamic brittle fracture. *Computer Methods in Applied Mechanics and Engineering* 2012; **217**–**220**(0):77–95.
2. Hofacker M, Miehe C. Continuum phase field modeling of dynamic fracture: variational principles and staggered FE implementation. *International Journal of Fracture* 2012; **178**(1–2):113–129.
3. Schlüter A, Willenbücher A, Kuhn C, Müller R. Phase field approximation of dynamic brittle fracture. *Computational Mechanics* 2014; **54**(5):1141–1161.
4. Miehe C, Schänzel LM, Ulmer Heike. Phase field modeling of fracture in multi-physics problems. Part I. Balance of crack surface and failure criteria for brittle crack propagation in thermo-elastic solids. *Computer Methods in Applied Mechanics and Engineering* 2015; **294**:449–485.
5. Miehe C, Hofacker M, Schänzel LM, Aldakheel F. Phase field modeling of fracture in multi-physics problems. Part II. Coupled brittle-to-ductile failure criteria and crack propagation in thermo-elastic-plastic solids. *Computer Methods in Applied Mechanics and Engineering* 2015; **294**:486–522.
6. Bourdin B, Francfort GA, Marigo JJ. The variational approach to fracture. *Journal of Elasticity* 2008; **91**(1–3):5–148.
7. Bouchbinder E, Goldman T, Fineberg J. The dynamics of rapid fracture: instabilities, nonlinearities and length scales. *Reports on Progress in Physics* 2014; **77**(4):046501.
8. Dally T, Weinberg K. The phase-field approach as a tool for experimental validations in fracture mechanics. *Continuum Mechanics and Thermodynamics* 2015:1–10.
9. Lancioni G, Royer-Carfagni G. The variational approach to fracture mechanics. A practical application to the French Panthéon in Paris. *Journal of Elasticity* 2009; **95**(1–2):1–30.
10. Freddi F, Royer-Carfagni G. Regularized variational theories of fracture: a unified approach. *Journal of the Mechanics and Physics of Solids* 2010; **58**(8):1154–1174.
11. Pham K, Amor H, Marigo JJ, Maurini C. Gradient damage models and their use to approximate brittle fracture. *International Journal of Damage Mechanics* 2011; **20**(4):618–652.
12. Sicsic P, Marigo JJ. From gradient damage laws to Griffith's theory of crack propagation. *Journal of Elasticity* 2013; **113**(1):55–74.
13. Li T, Marigo JJ, Guilbaud D, Potapov S. Variational approach to dynamic brittle fracture via gradient damage models. *Applied Mechanics and Materials* 2015; **784**:334–341.
14. Pham K, Marigo JJ, Maurini C. The issues of the uniqueness and the stability of the homogeneous response in uniaxial tests with gradient damage models. *Journal of the Mechanics and Physics of Solids* 2011; **59**(6):1163–1190.
15. Pham K, Marigo JJ. From the onset of damage to rupture: construction of responses with damage localization for a general class of gradient damage models. *Continuum Mechanics and Thermodynamics* 2013; **25**(2–4):147–171.
16. Mesgarnejad A, Bourdin B, Khonsari MM. Validation simulations for the variational approach to fracture. *Computer Methods in Applied Mechanics and Engineering* 2015; **290**:420–437.

17. Kuhn C, Schlüter A, Müller R. On degradation functions in phase field fracture models. *Computational Materials Science* 2015; **108**:374–384.
18. Bourdin B, Francfort GA, Marigo JJ. Numerical experiments in revisited brittle fracture. *Journal of the Mechanics and Physics of Solids* 2000; **48**(4):797–826.
19. Lorentz E, Kazymyrenko K. Application of a nonlocal damage law to model concrete fracture. *Computational Modelling of Concrete Structures* 2014:209–217.
20. Hesch C, Weinberg K. Thermodynamically consistent algorithms for a finite-deformation phase-field approach to fracture. *International Journal for Numerical Methods in Engineering* 2014; **99**(12):906–924.
21. Amor H, Marigo JJ, Maurini C. Regularized formulation of the variational brittle fracture with unilateral contact: numerical experiments. *Journal of the Mechanics and Physics of Solids* 2009; **57**(8):1209–1229.
22. Piero GD, Lancioni G, March R. A variational model for fracture mechanics: numerical experiments. *Journal of the Mechanics and Physics of Solids* 2007; **55**(12):2513–2537.
23. Miehe C, Hofacker M, Welschinger F. A phase field model for rate-independent crack propagation: robust algorithmic implementation based on operator splits. *Computer Methods in Applied Mechanics and Engineering* 2010; **199**(45–48):2765–2778.
24. Ambati M, Gerasimov T, de Lorenzis L. A review on phase-field models of brittle fracture and a new fast hybrid formulation. *Computational Mechanics* 2015; **55**(2):383–405.
25. Ciarlet PG, Nečas J. Injectivity and self-contact in nonlinear elasticity. *Archive for Rational Mechanics and Analysis* 1987; **97**(3):171–188.
26. Bourdin B, Larsen CJ, Richardson CL. A time-discrete model for dynamic fracture based on crack regularization. *International Journal of Fracture* 2011; **168**(2):133–143.
27. Larsen CJ, Ortner C, Süli E. Existence of solutions to a regularized model of dynamic fracture. *Mathematical Models and Methods in Applied Sciences* 2010; **20**(7):1021–1048.
28. Simone A, Askes H, Peerlings RHJ, Sluys LJ. Interpolation requirements for implicit gradient-enhanced continuum damage models. *Communications in Numerical Methods in Engineering* 2003; **19**(7):563–572.
29. Balay S, Abhyankar S, Adams MF, Brown J, Brune P, Buschelman K, Dalcin L, Eijkhout V, Gropp WD, Kaushik D, Knepley MG, McInnes LC, Rupp K, Smith BF, Zampini S, Zhang H. PETSc Users Manual. *Technical Report ANL-95/11 - Revision 3.6*, Argonne National Laboratory, 2015. (Available from: <http://www.mcs.anl.gov/petsc>) [Accessed on 1 December 2015].
30. Moré J, Toraldo G. On the solution of large quadratic programming problems with bound constraints. *SIAM Journal on Optimization* 1991; **1**(1):93–113.
31. Benson SJ, McInnes LC, Moré JJ. GPCG: A case study in the performance and scalability of optimization algorithms. *ACM Transactions on Mathematical Software* 2001; **27**(3):361–376.
32. CEA, EC. EUROPLEXUS: A Computer Program for the Finite Element Simulation of Fluid-Structure Systems under Transient Dynamic Loading. User's Manual. *Technical Report*, Commissariat à l'énergie atomique and European Commission, 2015. (Available from: <http://www-epx.cea.fr>) [Accessed on 1 December 2015].
33. Li T, Maurini C. *FEniCS (Dynamic) Gradient Damage*, 2015. (Available from: <https://bitbucket.org/litianyi/dynamic-gradient-damage>) [Accessed on 1 December 2015].
34. Logg A, Mardal KA, Wells G. *Automated Solution of Differential Equations by the Finite Element Method: The FEniCS book*, Vol. 84. Springer Science & Business Media, 2012.
35. Negri M. The anisotropy introduced by the mesh in the finite element approximation of the Mumford–Shah functional. *Numerical Functional Analysis and Optimization* 1999; **20**(9–10):957–982.
36. Lorentz E, Godard V. Gradient damage models: toward full-scale computations. *Computer Methods in Applied Mechanics and Engineering* 2011; **200**(21–22):1927–1944.
37. Vignollet J, May S, de Borst R, Verhoosel CV. Phase-field models for brittle and cohesive fracture. *Meccanica* 2014; **49**(11):2587–2601.
38. Pham K, Marigo JJ. Stability of homogeneous states with gradient damage models: size effects and shape effects in the three-dimensional setting. *Journal of Elasticity* 2013; **110**(1):63–93.
39. Kalthoff JF. Modes of dynamic shear failure in solids. *International Journal of Fracture* 2000; **101**(1–2):1–31.
40. Scherzinger WM, Dohrmann CR. A robust algorithm for finding the eigenvalues and eigenvectors of 3×3 symmetric matrices. *Computer Methods in Applied Mechanics and Engineering* 2008; **197**(45–48):4007–4015.
41. May S, Vignollet J, de Borst R. A numerical assessment of phase-field models for brittle and cohesive fracture: Γ -convergence and stress oscillations. *European Journal of Mechanics - A/Solids* 2015; **52**:72–84.
42. Hossain MZ, Hsueh CJ, Bourdin B, Bhattacharya K. Effective toughness of heterogeneous media. *Journal of the Mechanics and Physics of Solids* 2014; **71**:15–32.
43. Moreau K, Moës N, Picart D, Stainier L. Explicit dynamics with a non-local damage model using the thick level set approach. *International Journal for Numerical Methods in Engineering* 2015; **102**(3–4):808–838.
44. Fineberg J, Marder M. Instability in dynamic fracture. *Physics Reports* 1999; **313**(1):1–108.
45. Schardin H. Velocity effects in fracture. In: *B.L., Averbach et al.* (ed.). *Fracture* Wiley: New York, 1959; 297–330.
46. Haboussa D, Grégoire D, Elguedj T, Maigre H, Combescure A. X-FEM analysis of the effects of holes or other cracks on dynamic crack propagations. *International Journal for Numerical Methods in Engineering* 2011; **86**(4–5): 618–636.
47. Grégoire D, Maigre H, Réthoré J, Combescure A. Dynamic crack propagation under mixed-mode loading – Comparison between experiments and X-FEM simulations. *International Journal of Solids and Structures* 2007; **44**(20): 6517–6534.